Halide Perovskite Nanocrystal Emitters

Maning Liu, G. Krishnamurthy Grandhi, Sri Matta, Krishnaiah Mokurala, Aleksandr Litvin, Salvy Russo, and Paola Vivo*

The increasing attention on halide perovskite nanocrystals (PNCs) stems from their outstanding optoelectronic properties, especially the intriguing photoluminescence (PL) features. The high photoluminescence quantum yields (up to unity) of PNCs, and the tunability of their optical bandgaps by composition engineering and quantum confinement effects, account for the demonstrated great potential in several optoelectronic applications, such as light-emitting diodes (LEDs), phosphors, lasers, and photodetectors. However, despite the rapid growth of this research field, several questions are still left unanswered and there is room for further improving the luminescence performance, particularly for emerging lead-free PNC compositions. Herein, the recent advances in the light emission phenomena in PNCs are discussed. A special focus is given to the correlation between PL and phase transition, the dual-color emission, the tunability of the PL toward near-infrared (NIR), and the thermal quenching effect. The key research findings on LEDs, the major application of perovskite-based nanoscale emitters, are also outlined. Finally, the view on the most urgent challenges to be addressed is provided, with the intent of promoting a more profound understanding of PNC emission-related phenomena in the future.

1. Introduction

Since the first report on colloidal organometal halide perovskite nanocrystals (PNCs) by Schmidt et al., demonstrating an encouraging photoluminescence quantum yield (PLQY) of 20%,[1] metal halide PNCs have attracted ever-growing attention due to their remarkable optical and electronic properties.[2,3] PNCs are characterized by strong absorption coefficients, high charge carrier mobilities (1–10 $cm^2 V^{-1} s^{-1}$), up to near-unity PLQY, high emission color purity, and easily tunable photoluminescence (PL) emission in a wide spectral region (390–1050 nm[4]).[5–8] As a result, their potential for a broad range of applications, such as light-emitting diodes (LEDs),[9,10] solar cells,[11,12] photodetectors,[13,14] and lasers,[15] has been recently exploited with highly promising results.

The broad PL tunability of halide perovskites, through chemical composition engineering or quantum confinement, can be explained in terms of the electronic structure of these materials.[16] The conduction band (CB) of perovskites lies in the hybridized antibonding orbitals of the Pb 6p orbitals and in the outer p orbitals of the halide (5p for I, 4p for Br, and 3p for Cl), which tend to be p-like because of the high density of states (DOS) from the Pb contribution. On the other hand, the valence band (VB) lies in the hybridized antibonding states of the Pb 6s orbitals and in the same halide p-orbitals as for the CB.[16] Due to this electronic structure, the PL emission of halide PNCs can be modulated to enable a large set of energies/colors from near-UV to the whole visible and even to near-infrared (NIR) light, while also covering a range of bandwidths from narrow blue emission with high color focusing to broadband white-light with high color rendering index (CRI).[17]

The PL-related properties are certainly among the most intriguing features of PNCs. When compared with their bulk or single-crystal counterparts, PNCs display typically higher PLQY.[4] This can be attributed to the unique quantum confinement effect, which is one of the most effective ways to increase the radiative recombination rate, and hence the PLQY.

The origin of the luminescence in PNCs can be ascribed to either their inorganic or organic components. The inorganic parts are 1) the generated excitons (e.g., electron–hole pairs) that

Dr. M. Liu, Dr. G. K. Grandhi, Prof. P. Vivo
Faculty of Engineering and Natural Sciences
Tampere University
P.O. Box 541, FI-33014 Tampere, Finland
E-mail: paola.vivo@tuni.fi

Dr. S. Matta, Prof. S. Russo
ARC Centre of Excellence in Exciton Science
School of Science
RMIT University
Melbourne 3000, Australia

Dr. K. Mokurala
Department of Electronics Engineering
Incheon National University
Incheon 34958, South Korea

Dr. A. Litvin
The Laboratory "Optics of Quantum Nanostructures"
Center of Information Optical Technology
ITMO University
49 Kronverksky Pr., St. Petersburg 197101, Russia

realize the unlimited diffusion in the lattice in the form of free excitons, or 2) the bound excitons arisen from the interaction with lattice defects, or 3) the self-trapped excitons (STEs) originated from the so-called transient lattice deformations. All these possible pathways can contribute to the charge radiative recombination, which leads to the emission of photons.[18] In addition, the emission can also originate from the localized transitions upon the various ligands (organic) environment capping on a single metal cation either as an alloying element or as a dopant. For the organic components, the emission is mainly assigned to some chromophore groups, which could be excited either directly by incident light or indirectly upon internal energy transfer from the inorganic part.[19]

The profound understanding and engineering of the PL properties in halide PNCs are highly necessary to further strengthen their potential for diverse applications and to gain crucial insights on the kinetics of perovskite charge-carriers and on the role of perovskite's processing and structure on the kinetics.[20] Though the field of PNCs is advancing rapidly and with it also the understanding of the emission features of these materials, there are still a lot of unanswered questions and challenges to be solved. As of today, there are a significant number of review articles covering the synthesis, optoelectronic properties, and related applications of halide PNCs.[21–27] However, a comprehensive review with a specific focus on the luminescence properties of halide perovskite materials at the nanoscale is still missing and we want to fill this knowledge gap.

In this Review, we discuss the most recent research on the key factors enabling the emission tunability of halide PNCs. We do not attempt to comprehensively assess all the possible aspects of light emission in PNCs, rather preferring to focus on what we believe is the most important and timely research progress on PNCs PL engineering. Particularly, we aim at working out the correlation between structures and PL properties in halide PNCs. The influence of phase structural transition on PL emission of PNCs is the focus of Section 2 from both a theoretical and an experimental perspective. Following that, the direct–indirect transitions in the band structure are discussed and correlated to their induced dual-color emission in Section 3. In Section 4, we extensively overview the doping induced dual-color emission in the near-UV-to-visible range for halide PNCs that act as the host lattices. The tunability of the PNCs emission toward the NIR range is sequentially reviewed in Section 5. Section 6 comprehensively describes the effect of temperature on the structures of the PNCs in relation to their corresponding emission, also referred to as thermal quenching of PNCs PL or emission thermal quenching. In Section 7, we highlight some of the most important works on PNCs-based LEDs, which are the major application of luminescent halide PNCs. Finally, we provide our prospects for future research questions on the luminescence properties of PNCs to overcome the most critical remaining challenges.

2. Phase Transitions

The luminescence properties of halide PNCs are strongly influenced by their featured structural phases that generate diverse band structures. The phenomena of phase transition in halide PNCs can affect the PL, which is typically accompanied by spectral shape variations. In addition, it is well known that the phase transition in perovskite materials can be triggered by several factors such as temperature, pressure, and light.[28] This highlights the importance of thoroughly understanding the mechanisms how phase transition influences the PL properties of halide PNCs, while providing a key hint for the development of suitable applications in various environmental conditions. In general, stable 3D perovskite structures are obtained when the tolerance factor (t) is in the range of 0.76–1.13.[29] Thus, perovskites with t at the boundary of the range, e.g., $FAPbI_3$ ($t \approx 1$) and $CsPbI_3$ ($t \approx 0.8$), easily experience a phase transition at room temperature (RT) to more stable hexagonal and orthorhombic phases, respectively, which are often defined as nonemitting "yellow phases."[18] As the cubic phase is always stable at high temperatures, the phase transitions strongly rely on the operating temperatures. Halide PNCs crystallize into 3D phases at RT: 1) $MAPbI_3$ NCs are tetragonal; 2) $FAPbBr_3$, $MAPbBr_3$, and $FAPbI_3$ NCs are pseudocubic; 3) $CsPbBr_3$ and $CsPbI_3$ NCs are orthorhombic.[30] Recently, big attention has been paid to the 3D polymorphs of $CsPbI_3$ and $FAPbI_3$ NCs due to their featured NIR emission. However, both types of PNCs are metastable at RT due to their suboptimum A-site cations, i.e., Cs^+ is too small and FA^+ is too large. This issue has been termed as "perovskite red wall."[31] The formation of mixed-cation-based PNCs, such as $Cs_{1-x}FA_xPbX_3$ NCs, could effectively address the aforementioned issue while stabilizing their featured phase and retaining the corresponding PL properties.

Postsynthetic ligand engineering is well known as one way to induce phase transitions in as-formed halide PNCs. The most investigated case is the $CsPbBr_3 \rightarrow Cs_4PbBr_6$ PNC transition (3D → 0D).[32–35] For this phase transition, $PbBr_2$ is extracted from the 3D $CsPbBr_3$ PNCs by adding an excess amount of amines.[32] Udayabhaskararao et al. proposed a scheme of a reversible phase transition between $CsPbX_3$ (initial form) and Cs_4PbX_6 PNCs (converted form) (**Figure 1**a), by detecting two separated PL peaks after one transition cycle (Figure 1b), which were attributed to the segregation of the back-converted particles into Br-rich and I-rich particles.[33] Chen et al. controlled the phase transition between 3D $CsPbBr_3$ and 0D Cs_4PbBr_6 by tuning the amount of ligands upon a facile ligand-assisted supersaturated recrystallization synthetic route, producing intense green luminescence with PLQYs up to 80% and 45% for 3D $CsPbBr_3$ and 0D Cs_4PbBr_6, respectively.[34] They observed that the PL lifetime (≈ 13 ns) of Cs_4PbBr_6 is much longer than that (≈ 6 ns) of $CsPbBr_3$ (Figure 1c,d) and photoblinking is also easily detected in 0D PNCs after the phase transition (Figure 1e). Another type of phase transition is from 3D $CsPbBr_3$ to 2D $CsPb_2Br_5$, which can be triggered either by a $PbBr_2$-rich environment ($CsPbBr_3 + PbBr_2 \rightarrow CsPb_2Br_5$)[36] or by extracting Cs^+Br^- ($2CsPbBr_3 \rightarrow CsPb_2Br_5 + Cs^+Br^-$) from the original 3D PNCs.[37] By following the former case, Li et al. synthesized 2D $CsPb_2Br_5$ nanosheets (NSs) in a tetragonal phase by attaching 3D orthorhombic $CsPbBr_3$ nanocubes in an orientation from octagonal to square in the lateral direction while realizing a shape evolution.[36] The authors observed a gradual decrease in the emission intensities with the increasing reaction time (toward $CsPb_2Br_5$ NSs), suggesting that the as-formed 2D NSs are PL inactive with an indirect bandgap of 2.979 eV based
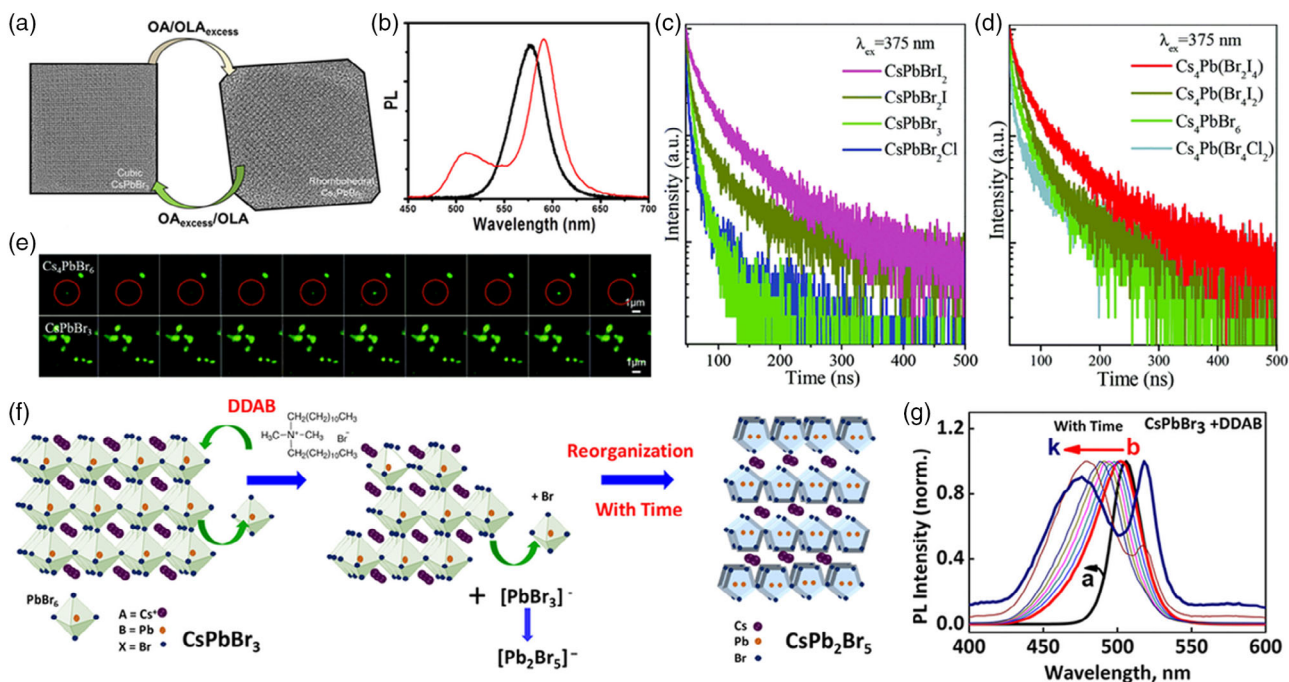
Figure 1. a) TEM images of cubic CsPbBr$_3$ to Cs$_4$PbBr$_6$ PNCs (from left to right, respectively) by means of addition of an excess of oleic acid/oleylamine for the forward reaction and the addition of oleic acid for the backward reaction. b) PL spectra upon back-and-forth transformation of a mixed halide perovskite through the Cs$_4$PbX$_6$ phase. The PL spectra of initial CsPbBr$_{1.5}$I$_{1.5}$ PNCs in black and that of segregated Br-rich and I-rich CsPbBr$_{3-x}$I$_x$ PNCs in red after one transformation cycle. Reproduced with permission.[33] Copyright 2017, American Chemical Society. TRPL decay curves of c) CsPbX$_3$ and d) Cs$_4$PbX$_6$ (X = Cl/Br, Br, Br/I) samples. e) The frequency flashing diagrams of the Cs$_4$PbBr$_6$ and CsPbBr$_3$ particles over time (from left to right) upon laser excitation at a wavelength of 405 nm; the photoblinking phenomena for a typical Cs$_4$PbBr$_6$ particle are marked by red circles. Reproduced with permission.[34] Copyright 2018, The Royal Society of Chemistry. f) Schematic representation of ligand-assisted exfoliation and transformation of cubic CsPbBr$_3$ PNCs to tetragonal CsPb$_2$Br$_5$ NSs. g) Normalized PL spectra (excitation wavelength 380 nm) recorded with a time interval of 1 min after the addition of DDAB (250 μM) to CsPbBr$_3$ PNCs in toluene: a) before adding DDAB and b–k) after addition of DDAB. Reproduced with permission.[37] Copyright 2018, American Chemical Society.

on density functional theory (DFT) simulation results. On the other hand, Balakrishnan et al. used the dodecyl dimethylammonium bromide (DDAB) ligand to induce the phase transition of CsPbBr$_3$ nanocrystals into 2D CsPb$_2$Br$_5$ NSs accompanied by morphological changes (**Figure 2**f).[37] Interestingly, the DDAB ligand could gradually exfoliate the [PbBr$_6$]$^{4-}$ octahedra of CsPbBr$_3$ as a function of time, resulting in a blue shift in the absorption spectra and band edge (BE) emission. At long reaction times, the evolution of a subemission band centered at 523 nm was observed (Figure 2g), which contributed to significantly reduce the PLQY from 70% to 4%.

In addition to the ligand-assisted phase transition, some other factors can also lead to the solid-state phase change in halide PNCs, i.e., light,[38] pressure,[39] heat,[40] and water.[41] Shen et al. monitored the dynamic process of the light-induced phase transition from tetragonal CsPb$_2$Br$_5$ to orthorhombic CsPbBr$_3$ upon continuous illumination.[38] The starting tetragonal CsPb$_2$Br$_5$ PNCs showed a weak emission intensity due to their indirect bandgap, and then with the increase in illumination time, they gradually transformed into CsPbBr$_3$ with an evidently enhanced emission intensity. However, obvious photonic damage occurred upon the illumination time of 30 min, leading to a decrease in PL intensity that was still stronger than that of the original tetragonal CsPb$_2$Br$_5$ PNCs.[38] Alternatively, Xiao et al. introduced high

pressure to tune the optical and structural properties of CsPbBr$_3$ PNCs, in which an isostructural phase transition in terms of the *Pbnm* space group took place.[39] The emission peak of CsPbBr$_3$ PNCs exhibited a red shift while gradually turned broad with the increasing pressure (from 1 atm to 1.36 GPa). Furthermore, the PL intensity decreased rapidly under the compression at 1.21 GPa, due to the structure-related change. Their pressure-dependent time-resolved PL (TRPL) data showed that the charge carrier lifetime of CsPbBr$_3$ PNCs was extended from 12.6 ns in ambient condition to 14.7 ns upon the compression to 1.03 GPa, indicative of a pressure-driven decrease in oscillator strength that is consistent with the changes in PL intensity.[39] More interestingly, Wu et al. proposed a novel CsX-stripping (X = Cl, Br, I) mechanism that enables an efficient phase transition of nonluminescent 0D Cs$_4$PbX$_6$ PNCs to highly luminescent 3D CsPbX$_3$ PNCs upon an interfacial reaction with water in a different phase.[41] The water-induced phase transition could effectively tune the PL wavelength to cover the full visible range while narrowing the emission bandwidth with an enhanced PLQY up to 75%. The converted 3D CsPbX$_3$ PNCs also show improved photostability against moisture due to the surface passivation at the interface between the nonpolar phase and water.

Several theoretical studies by, e.g., DFT calculations have been implemented to predict and validate the influence of phase
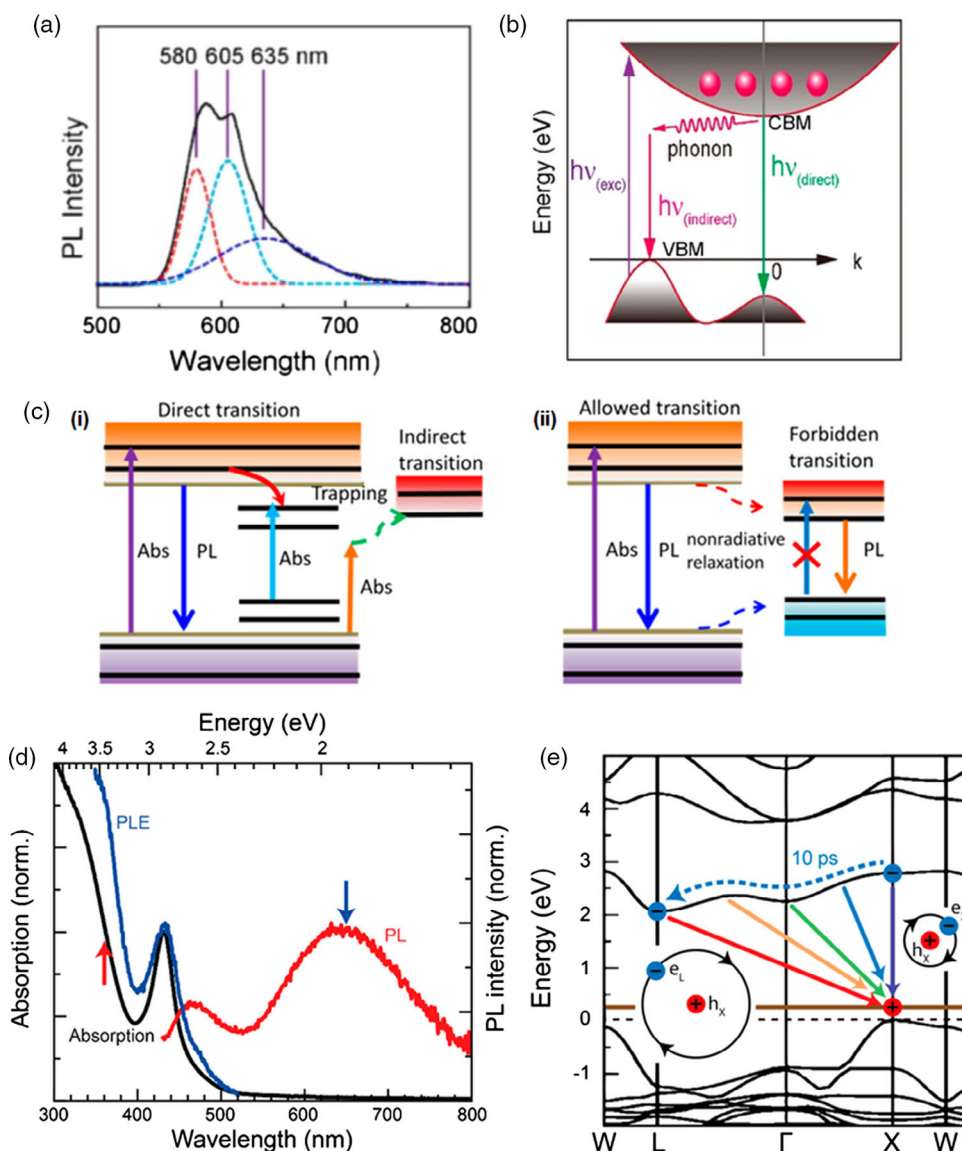
Figure 2. a) Deconvolution of the PL profile of $Cs_3Bi_2I_9$ PNCs at RT, showing three peaks centered at 580, 605, and 635 nm. b) Proposed recombination pathways in $Cs_3Bi_2I_9$ PNCs. Reproduced with permission.[63] Copyright 2017, American Chemical Society. c) Charge carrier dynamics model of (i) indirect bandgap double perovskite $Cs_2AgIn_xBi_{1-x}Cl_6$ ($x = 0$, 0.25, and 0.5) PNCs and (ii) direct bandgap double perovskite $Cs_2AgIn_xBi_{1-x}Cl_6$ ($x = 0.75$ and 0.9) PNCs. Reproduced with permission.[64] Copyright 2018, American Chemical Society. d) Linear absorption, PL (excited at 365 nm), and photoluminescence excitation (PLE) (detected at 650 nm) spectra of $Cs_2AgBiBr_6$ PNCs dispersed in toluene. e) Scheme depicting the transfer of direct to indirect bound excitons of $Cs_2AgBiBr_6$ double PNCs, whereby the binding energy reduces. Reproduced with permission.[65] Copyright 2020, American Chemical Society.

structure change on the corresponding PL properties in PNCs. Jang et al. predicted the phase-dependent structures (cubic, C, and tetragonal, T, phases) of $MAPbX_3$ PNCs with the help of DFT, and then calculated their structural properties (e.g., lattice parameters and atomic positions) with corresponding bandgaps. All the properties were eventually related to the direct or indirect change in the PL properties. In particular, the authors performed the DFT calculations (projector augmented-wave (PAW)[42] method along with van der Waals interaction was included in this assessment through the Perdew–Burke–Ernzerhof [PBE]-D2 calculation[43]) to predict possible C/T phases configurations for $MAPbBr_{3-x}Cl_x$ and $MAPbBr_{3-x}I_x$ with $x = 0$, 1, 2, and 3 systems

(see the detailed discussion in the study by Jang et al.[43]). According to DFT evaluations, all the studied configurations showed direct bandgaps. It was also found that the T phase is marginally (<0.01 eV atom^{-1}) more stable than the C phase, however, indicating that both structures can exist at RT. Regarding the structural compositional-dependent PL decay lifetime of $MAPbX_3$ PNCs, the authors proposed that the PNCs with T phase structures exhibit more efficient charge separation and slower recombination rate compared with the case of C phase structures, due to the staggered geometry of $[PbX_3]^-$ in T phase that possesses the quasicubic structure. Therefore, the presence of the eclipsed C-phase structures can effectively reduce the PL lifetime, as it has been

observed for MAPbBr$_{3-x}$Cl$_x$ PNCs.[43] The observed longest PL decay lifetime of MAPbBr$_{3-x}$I$_x$ PNCs at $x = 2$ is mainly due to the lack of C phase structures. Thus, DFT analysis could well support and explain the possible reasons for the experimental PL data. A similar DFT study elucidated that the bandgap of MAPbI$_3$ PNCs was influenced by the transition between orthorhombic (1.90 eV) and tetragonal (1.82 eV) phase structures, and this variation also occurred due to the MA$^+$ distribution.[44] Their DFT results clearly indicate that the interaction between the MA$^+$ and the inorganic part can affect the crystal structure, which tailors the electronic structure and the bandgap accordingly. Though the calculated absorption spectrum appeared to be similar in shape to the experimental one, the excitonic peaks showed a red shift after the phase transition from orthorhombic to tetragonal structures. Although Geng et al. did not report the simulated PL, a similar corresponding red shift in the PL spectrum has been reported in the study by Schötz et al.[45]

3. Direct–Indirect Transitions Induced Dual-Color Emission

In addition to the phase structural transitions, the band structure changes also enable the tuning of PL properties in PNCs. Direct–indirect transitions are one of the featured characteristics in the band structure of perovskite materials, inducing a so-called "dual-color emission" that consists of two distinguishable emission bands integrated into one PL spectrum. This phenomenon has been initially reported for many perovskites in single or bulk crystals.[46–48] However, still several disputes exist regarding the origins and mechanisms of this featured luminescence property. The reabsorption effect has been widely highlighted as a key enabler of the dual-color emission.[49–53] However, this emission feature can be also correlated to the Rashba effect induced by the centrosymmetry breaking by the perovskite's organic cations.[54,55] In addition, the grain size of conventional CH$_3$NH$_3$PbBr$_3$ bulk crystals can also determine which band structure dominates the overall PL spectra in between different structural phases (e.g., tetragonal-to-orthorhombic phase transition) at low temperature (e.g., 40–50 K), generating a dual-color emission when the same weight in both bands is achieved upon an optimum grain size of about 100 nm.[56] Recently, Wu et al. clarified that dual-color emission is even a common character of all lead halide perovskites, but the relative intensity of the low-energy peak (i.e., at longer wavelength) strongly depends on the surrounding conditions, such as the environmental temperature, and can lead to a nondistinguishable second peak in some cases.[57] The authors confirmed the existence of indirect tail states below the direct transition edge due to the dynamic Rashba splitting effect in APbBr$_3$ (A = CH$_3$NH$_3^+$, CH(NH$_2$)$_2^+$, Cs$^+$) single crystals, which was originated from the thermal polar distortions of the PbBr$_6$ octahedra at increased temperatures. These thermal polar variations and their corresponding indirect tail states in lead-based perovskite single crystals lead to low PLQY and to the reduction of charge carrier lifetimes with inefficient charge separation even at low temperatures.[57]

Similarly, the phenomenon of dual-color emission in halide PNCs has also attracted extensive attention as one of the key luminescence properties, as the engineering of dual-color emission can enable a wider emission spectral range in a single type of nanocrystal, which in turn is beneficial to, e.g., achieve a white light, or even a NIR light, emitter. In this and following section, we provide a comprehensive review of the dual-color emission of PNCs from two mainstream views, namely direct–indirect transitions and doping induced dual-color emission in UV–vis range, respectively. Additional studies on dual-color emission related to the NIR range will be discussed in Section 5.

It is well known that lead halide PNCs possess a unique 3D perovskite structure and direct bandgap nature, resulting in near-unity PLQY with one distinguishable emission peak.[2,3,9,58] Due to the toxicity of Pb element, air-stable lead-free PNCs using Bi^{3+}, Sb^{3+}, and the lead-free double perovskites (e.g., Cs$_2$AgBiBr$_6$ or Cs$_2$AgInCl$_6$) have recently attracted more attention.[59–62] Interestingly, these reported lead-free PNCs generally show an indirect bandgap character, resulting in a clear sub-bandgap absorption that is correlated with indirect transitions. Accordingly, the coexistence of direct and indirect transitions in some lead-free PNCs could potentially induce the dual-color emission feature. Zhang et al. first reported a dual-color direct–indirect transition nature of Cs$_3$Bi$_2$I$_9$ PNCs with an observed double-spectral characteristic in the emission profile with two distinguishable peaks centered at 580 and 605 nm, respectively (Figure 2a).[63] Based on the temperature-dependent PL and transient absorption (TA) spectroscopy studies, the authors proposed a scheme of charge recombination pathways in Cs$_3$Bi$_2$I$_9$ PNCs (Figure 2b). After the excitation, the generated hot electrons at the excited state directly cool to the conduction band minimum (CBM) and then recombine with holes in the valence band maximum (VBM), resulting in the direct BE emission at 605 nm. On the other hand, the indirect bandgap transitions can be initiated upon the assistance of phonons, generating a 580 nm emission that competes with the direction transition process. The presence of these extra nonradiative recombination pathways could be the key reason resulting in the low PLQY for bismuth-based PNCs, which can be facilitated by the indirect bandgap.[63] Driven by the direct–indirect nature of the bandgap in lead-free PNCs, Yang et al. reported fully inorganic lead-free double-perovskite (DP) nanocrystals, i.e., Cs$_2$AgIn$_x$Bi$_{1-x}$Cl$_6$, whose bandgap could be effectively tuned from indirect transitions ($x = 0$–0.5) toward direct transitions ($x = 0.75$ and 0.9).[64] The tailored PNCs with direct bandgap show lower sub-bandgap trap states and more than five times higher PLQY (36.6%) compared with that of Cs$_2$AgBiCl$_6$ PNCs with indirect bandgap. The observed dual-color emission nature consists of one band-edge violet emission and one bright orange emission centered at 570 nm originating from the direct transition. Based on a comprehensive study of TRPL, TA, and DFT calculations, the authors formulated an overall charge carrier dynamics model of the indirect and direct bandgap of the investigated Ag–Bi-based DP PNCs (Figure 2c). Those PNCs with indirect bandgap present both high-energy direct transition and indirect transitions, which need the assistance of phonons and thereby lead to a low absorption coefficient and PLQY. For direct bandgap nanocrystals, the sub-bandgap trap-state transition is negligible, achieving a high PLQY close to the BE. Moreover, the excited electrons in the allowed state relax to the forbidden states through a swift nonradiative pathway, which only influences the absorption but does

**ADVANCED
SCIENCE NEWS**

www.advancedsciencenews.com

**ADVANCED
PHOTONICS
RESEARCH**
Open Access

www.adpr-journal.com

not change the relaxation of the excitons, eventually generating an orange emission.[64] Recently, Dey et al. observed a high energetic emission caused by the direct bandgap of $Cs_2AgBiBr_6$ PNCs, in addition to the intrinsic emission from the indirect bandgap transition (Figure 2d).[65] They attributed the former emission to the radiative recombination of direct bound excitons, exhibiting nearly 1 eV red shift within 10 ps timescale after the photoexcitation due to the electron intervalley scattering effect and thus resulting in a transfer of direct to indirect bound excitons (Figure 2e). These direct bound excitons feature a huge oscillator strength, leading not only to a distinguishable absorption peak near the BE but also to the generation of emission at the direct bandgap transition, although there is an intervalley scattering process.[65] Overall, the characteristics of direct and indirect transitions and related charge carrier dynamics in lead-free double PNCs still require urgent exploration, to expand the insights of the luminescence properties (e.g., dual-color emission) and thus boost the further development of optoelectronic devices.

4. Doping-Induced Dual-Color Emission in the UV-Vis Range

In addition to direct–indirect transitions induced dual-color emission, doping engineering is an alternative way to trigger the generation of a similar PL emission feature. The doping with metal cations in a host lattice has been well developed for conventional semiconductor nanocrystals, enabling effective tuning of the optical properties by combining both the quantum confinement effect of the host nanocrystals and the luminescence features (generally a dual-color emission feature) of the dopant ions.[66] As the host lattices, halide PNCs have been widely investigated for integrating the extrinsic emissive metal ions, mainly including divalent and trivalent cation dopants.

4.1. Divalent Dopants

As one of the most explored extrinsic divalent dopants in conventional semiconductor nanocrystals, Mn^{2+} ions have been successfully incorporated into the cesium lead halide PNCs. The dual-color emission feature displayed by the Mn-doped $CsPbX_3$ PNCs is ascribed to the spin-forbidden $^4T_1 \rightarrow {}^6A_1$ d–d transition of Mn^{2+} ions at about 600 nm, in addition to the BE emission of the host (**Figure 3**a).[67] From a structural point of view, it is imperative to prove the incorporation of Mn^{2+} into the lattices of the host PNCs that leads to the change in their corresponding PL characteristics. Due to the substitution of Pb^{2+} with smaller Mn^{2+} in the lattices of $CsPbX_3$ quantum dots (QDs), a lattice distortion or contraction could be induced in the octahedral coordination circumstance. Zou et al. simulated the 3D stacking diagrams of $CsPbBr_3$:Mn QDs (2.08 mol% doping) (Figure 3b), showing that the bond length of Mn—Br (2.666 Å) is much shorter than that of the first (3.382 Å) and second (3.034 Å) adjacent or normal (3.003 Å) Pb—Br bonds.[68] These lattice distortions can be also observed in high-resolution transmission electron microscopy (TEM) images for selected $CsPbBr_3$:Mn QDs in comparison with the host QDs without Mn doping. The authors demonstrated the Mn-doping concentration-dependent PL emission of as-formed $CsPbCl_3$:Mn NCs (Figure 3c,d),

showing a declining trend after an initial rise in PL intensity of the excitonic emission (centered at 404 nm). This emission tuning provided an overall color output from blue to orange-red that could be observed even by the naked eye (Figure 3e). Later, Bai et al. also confirmed the successful incorporation of Mn^{2+} into the lattices of the same host system ($CsPbCl_3$:Mn NCs), by observing a clear peak shift to a higher angle compared with the case of undoped one in their X-ray diffraction (XRD) analysis. Interestingly, they observed a tendency of a blue shift in the PL spectra of the BE emission from the host PNCs with the increased Mn-doping amount, ascribed to the effect of Mn^{2+} tailoring the host electronic band structure.[69]

There are several factors influencing the tuning of the PL properties for both the host PNCs and the dopants themselves, i.e., additives, temperature, anion exchange, and photoinduced doping. Adhikari et al. chemically tailored the dopant emission in Mn-doped $CsPbCl_3$ PNCs by introducing alkylamine hydrochloride (RNH_3Cl) as an active chlorinating agent for controlling the Mn-doping degree from 1% to 8% against Pb content and consequently tuning the Mn d–d emission intensity. The maximum PLQY of their best sample was about 27% with a Mn-doping concentration of 1.3%, and the excited-state decay of the Mn emission at 585 nm exhibited a long lifetime of about 1.4 ms, which is a typical timescale for Mn emission in d–d transition.[70] Ghosh et al. and Wang et al. nearly simultaneously reported the temperature-dependent variation of emission intensity and emission wavelength of both host PNCs ($CsPbCl_3$) and Mn dopants ranging from tens of kelvin to more than 300 K.[71,72] They observed the blue shift of the emission peak position with the increasing temperature (Figure 3f,g), attributed to the interplay between the electron–phonon renormalization and the thermal expansion. Ghosh et al. found that the PL intensity of Mn^{2+} diminishes with the increasing temperature up to 125 K, due to the thermal quenching induced by the thermal ionization of optically excited carriers. Afterward the dopant emission intensity increases again with the rising temperature, mainly resulting from the electrons captured by Mn^{2+} ions from local state energy levels (Figure 3h). The same report also investigated the temperature-dependent TRPL of Mn emission with the variable lifetimes from ≈1262.1 to ≈7.5 μs while decreasing the temperature from 250 to 70 K, ascribed to the interaction between the exciton and the surface state. Moreover, Mn-doped $CsPbCl_{3-x}Br_x$ or Mn-doped $CsPbBr_3$ PNCs could be obtained via either an anion exchange reaction or direct synthesis using $MnBr_2$ as the Mn precursor. Xu et al. investigated the composition and temperature dependence of Mn^{2+} to exciton emission intensity ratios for mixed halide $CsPbCl_{3-x}Br_x$ PNCs ($x = 0$–1.18) (Figure 3i).[73] By fixing the Mn-doping amount to 2.8%, with the replacement of Cl^- by Br^-, the PLQY increases up to about 60%, and the excitonic lifetime of the BE emission in the range of 403–442 nm is also prolonged from 0.5 to 12.6 ns (Figure 3j,k). The authors successfully controlled the exciton-to-Mn^{2+} transfer efficiency by varying the Br/Cl ratio. The efficiency first increases with an initial increasing Br^- in the structure upon a combined effect of slower exciton decay and faster energy transfer from the host to Mn^{2+} ions. Along with the narrower bandgap with more substitution of Br^-, back energy transfer from Mn^{2+} to host band states starts to dominate the overall exciton dynamics and leads to a sharp reduction of the relative Mn^{2+} emission intensity.
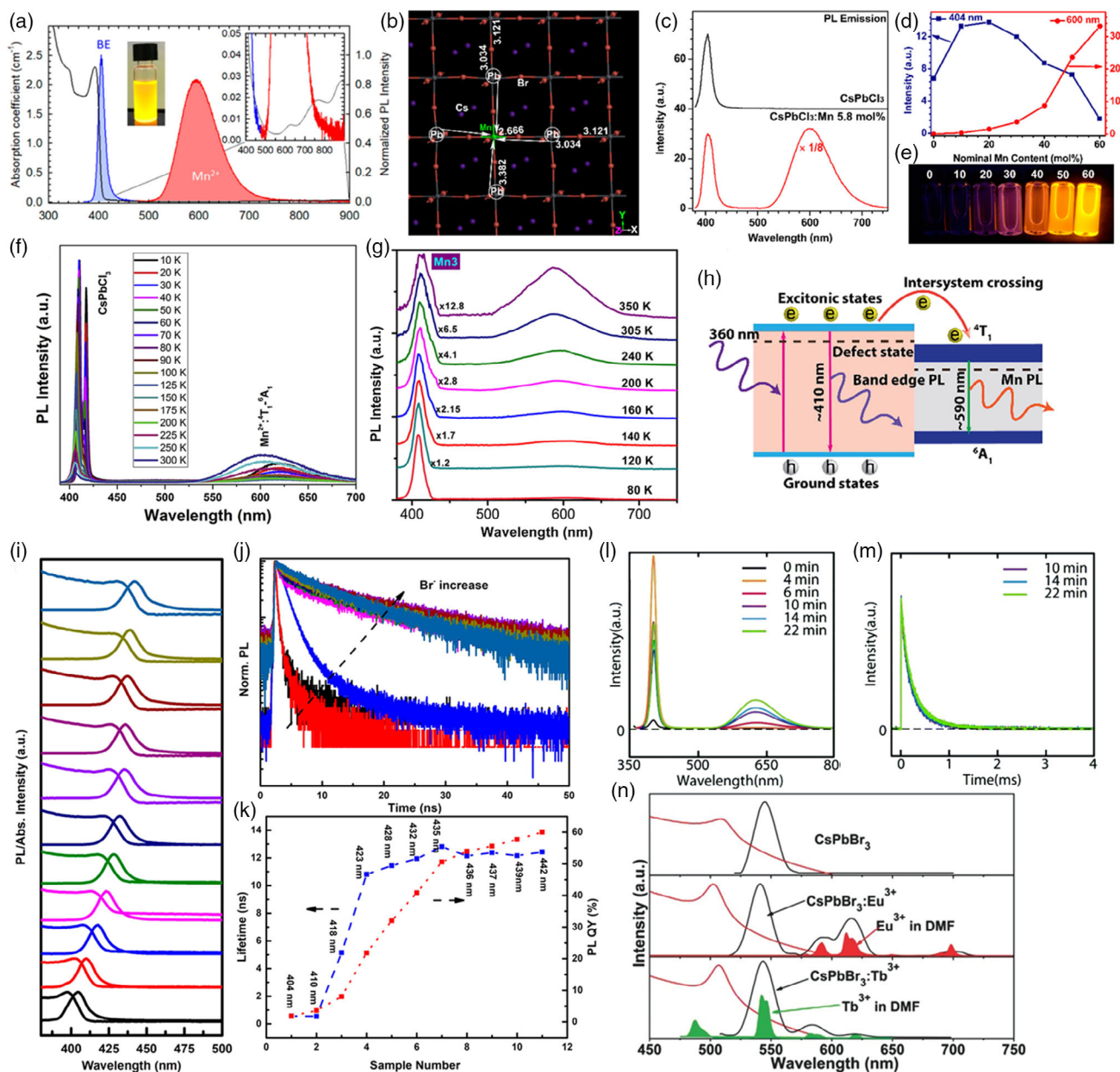
Figure 3. a) Optical absorption (black line) and PL spectra of Mn/CsPbCl$_3$ PNCs (4% doping level) under 390 nm excitation in toluene solution. The BE and Mn-related PL bands are highlighted by blue and red shading, respectively. A photograph of the solution under 365 nm excitation highlights the dominant yellow color due to Mn^{2+} emission with respect to BE PL. Reproduced with permission.[67] Copyright 2017, American Chemical Society. b) Calculated 3D stacking diagram of a CsPbBr$_3$:Mn (2.08 mol % doping) NCs using first-principle calculations based on DFT, showing the lattice contraction in the (001) lattice plane of an orthorhombic perovskite CsPbBr$_3$ crystal induced by Mn^{2+} doping. c) Comparison of the PL spectra for CsPbCl$_3$ QDs without and with Mn doping (5.8 mol %) upon an excitation at 362 nm. d) PL intensities for excitonic or Mn emissions of CsPbCl$_3$:Mn QDs centered at 404 and 600 nm as a function of the nominal doping concentration of Mn^{2+} ions, and their corresponding e) PL emission photographs in cyclohexane solution under 362 nm UV lamp irradiation. Reproduced with permission.[68] Copyright 2017, American Chemical Society. f) Temperature-dependent PL spectra of the Cs(Pb$_{0.5}$Mn$_{0.5}$)Cl$_3$. Reproduced with permission.[72] Copyright 2020, Elsevier B.V. g) Temperature-dependent PL spectra of 3% Mn-doped CsPbCl$_3$ PNCs film. PL spectra at different temperatures are scaled up appropriately to enable better comparison. h) Energy band diagram and PL emission mechanisms of CsPb$_x$Mn$_{1−x}$Cl$_3$ PNCs. The horizontal dashed lines represent the defect-related energy levels. Reproduced with permission.[71] Copyright 2019, Elsevier Inc. Evolution of PL properties of CsPbCl$_{3−x}$Br$_x$ PNCs at 300 K as a function of x (x is varied from 0 to 1.18 estimated from the position of the exciton peak): i) Absorption and PL spectra of CsPbCl$_{3−x}$Br$_x$ PNCs with different x (λ_{ex} = 355 nm); j) PL decay curves of the exciton emission for CsPbCl$_{3−x}$Br$_x$ PNCs plotted on semilogarithm scale (λ_{ex} = 376 nm, pulse width = 65 ps); k) PLQY and exciton emission lifetime of CsPbCl$_{3−x}$Br$_x$ PNCs upon increasing x. Reproduced with permission.[73] Copyright 2018, American Chemical Society. l) PL spectra and m) time-dependent Mn luminescence intensity of CsPbCl$_3$ nanocrystals undergoing the photoinduced Mn doping by a UV LED at the intensity of 14 mW cm$^{−2}$ and varying photoexcitation times. Reproduced with permission.[75] Copyright 2019, The Royal Society of Chemistry. n) The absorption and PL spectra of CsPbBr$_3$ PNCs (top), CsPbBr$_3$:Eu^{3+} NCs (middle), and CsPbBr$_3$:Tb^{3+} PNCs (bottom). The red lines represent absorption spectra, and black lines represent PL spectra. The red and green shades represent emission spectra of Eu^{3+} and Tb^{3+}, respectively. Reproduced with permission.[86] Copyright 2017, WILEY-VCH.

**ADVANCED
SCIENCE NEWS**
www.advancedsciencenews.com

**ADVANCED
PHOTONICS
RESEARCH**
Open Access
www.adpr-journal.com

Chen et al. synthesized Mn-doped $CsPbX_3$ (X = Br, Cl) QDs at RT by introducing a precursor of dimethyl sulfoxide (DMSO)-$MnBr_2/PbX_2$ composite, achieving a relatively high PLQY of the Mn^{2+} emission ($\approx$36.7%), which is comparable with that of QDs obtained through the conventional hot-injection method.[74] By changing the $PbBr_2/PbCl_2$ ratio, the authors were able to tune the energy transfer rate from the BE to the Mn^{2+} excited state in the range of 0.006–20.42 $\times 10^7 s^{-1}$.

More interestingly, Qiao et al. demonstrated a postsynthesis photoinduced Mn doping in $CsPbX_3$ (X = Br, Cl) PNCs, while still preserving the anisotropic morphology of the initial PNCs after the photoinduced doping.[75] The average lifetime of Mn emission is gradually extended with continued photoinduced Mn doping from 0.3 to 1 ms, indicative of the larger Mn—Mn distance and weaker effect of Mn-Mn exchange coupling on Mn emission under the higher photoexcitation (Figure 3l,m). It is noted that, compared with Cl- or Br-based PNCs, it is more difficult for iodide-based ones (e.g., $CsPbI_3$ PNCs) to display the Mn-doping effect of dual-color emission, mainly due to the negligible Mn emission intensity. Such weak emission is attributed to the BE position of host $CsPbI_3$ PNCs that is rather lower than Mn^{2+}-based transitions, thus not providing sufficient driving force for the energy transfer.[76] Akkerman et al. maximized the PLQY of $CsPbI_3$ PNCs up to 82% by doping Mn^{2+} with a 10% concentration of Pb content, while slightly extending the excitonic lifetime from 14 to 17 ns at 680 nm peak emission.[77] They found that the $CsPb_xMn_{1-x}I_3$ PNCs can preserve the identical optical features and crystal structure as the parent α-$CsPbI_3$ system; however, the Mn-doped PNCs films were stable for periods over a month, whereas the α-$CsPbI_3$ NCs without Mn doping degraded into the yellow nonemitting δ-$CsPbI_3$ phase within a few days. The enhanced stability of Mn-doped $CsPbI_3$ PNCs originates from a small decrease in the lattice constants slightly improving the Goldsmith tolerance factor, along with an enhancement in the cohesive energy. Furthermore, He et al. precipitated Mn-doped $CsPb(Cl/Br)_3$ QDs into phosphosilicate glass using a heat-treatment method, resulting in long excitonic lifetimes for both host emission ($\approx$122 ns) at about 520 nm and Mn emission ($\approx$2.85 ms) at around 600 nm.[78] The Mn-doped $CsPb(Cl/Br)_3$ QDs glass shows good thermal and light stability, by continuing to emit strong orange-red fluorescence after a long-term placement in the air. In addition to the fully inorganic halide PNCs, according to Ba et al., the dual-color emission induced by Mn doping could be also observed for some water-stable 2D organic–inorganic halide PNCs as the host, i.e., $(PEA)_2PbBr_4$ nanoplates (PEA = phenethylamine).[79] This work demonstrates that the proper steric hydrophobic π-conjugated PEA molecules at A site can improve the water stability of hybrid halide PNCs, providing significant hints on how to stabilize the high-performing 2D perovskite-based LEDs and luminescent indicators.

In addition to the well-investigated Mn-doping induced dual-color emission in halide PNCs, there are some other divalent dopants that have also been incorporated into the host PNCs. Xing et al. successfully synthesized Mn^{2+} and Ni^{2+} codoped $CsPbCl_3$ PNCs by maximizing the PLQYs of Mn^{2+} emissions centered at 600 (from Mn^{2+}-based transition) and 620 nm (from Ni^{2+}-based transition) up to 70% and 39%, respectively.[80] The introduction of Ni^{2+} can effectively reduce the defect and trap

states formed in $Mn:CsPbCl_3$ PNCs while enhancing the formation energies of Mn doping to improve Mn doping yield for boosting the Mn^{2+} emission efficiency, as revealed by the DFT calculations. van der Stam et al. proposed a postsynthetic cation exchange method by doping $CsPbBr_3$ PNCs with three types of divalent cations, i.e., Sn^{2+}, Cd^{2+}, and Zn^{2+}, leading to a blue shift of the emission bands without losing the high PLQYs (>60%) and narrow emission bandwidth.[81] The authors assigned the blue shift to the contraction of the perovskite lattice that stems from the incorporation of smaller divalent doping cations, making the Pb—halide bonds shorter so as to enhance the interaction between Pb and Br orbitals.

4.2. Trivalent Dopants

Trivalent metal ions have also been used for the so-called heterovalent doping in halide PNCs. Begum et al. proposed an in situ doping approach for $CsPbBr_3$ PNCs with Bi^{3+} ions via hot injection to accurately modulate the band structure and the excited state dynamics.[82] They observed that, at a low doping concentration of Bi^{3+} (e.g., <0.25%), a red shift of PL spectrum arises with fewer impurity levels or trap states "below" the first electronic state, i.e., $1S_e$, of the CB. At high-doping concentrations (e.g., 0.8–2.1%), a blue shift is noted instead, corresponding to the evolution of the trap states "above" the $1S_e$ state. This Bi^{3+} doping induced a band structure change that can effectively promote the charge transfer kinetics at the interface of PNCs and charge acceptors. Moreover, rare-earth ions have been extensively utilized as dopants in metal oxides, II–VI semiconductors, and $NaYF_4$, showing diverse energy transitions and accordingly outstanding PL emissions covering from UV-to-visible light, toward the infrared range.[83,84] After Zhou et al. first reported various lanthanide ion-doped PNCs,[85] Hu et al. doped rare-earth ions Eu^{3+} and Tb^{3+} into $CsPbBr_3$ PNCs using a one-pot ultrasonication method, exhibiting the dual-color emission in the visible range up to 700 nm (Figure 3n) from the host PNCs and doped rare-earth ions, respectively.[86] Their TRPL studies demonstrated that both the lifetimes of Eu^{3+} (0.76 to 0.37 ms) and Tb^{3+} (1.81 to 1.63 ms) emissions in $CsPbBr_3$ PNCs decreased compared with those of their pure cation states in the solvent. This suggests that there could be an extra decay pathway for rare-earth ions with the possible energy transfer from rare-earth dopants to the host PNCs. Later, Yao et al. enhanced the PL/electroluminescence (EL) efficiency of $CsPbBr_3$ PNCs by doping heterovalent Ce^{3+} ions through a facile hot-injection method, presenting a nearly overlapping dual-color emission centered at 516 and 510 nm for the host PNCs and the Ce^{3+} dopant, respectively.[87] The authors found that, by increasing the doping amount of Ce^{3+} up to 2.88% of Pb content, the PLQY of Ce^{3+}-doped $CsPbBr_3$ PNCs achieved the highest value of 89%, which was two times higher than that of undoped ones. Their ultrafast TA and TRPL experiments suggest that Ce^{3+} doping can effectively tune the PL kinetics while enhancing the PLQY of doped $CsPbBr_3$ PNCs. Chen et al. first doped another type of rare-earth trivalent ions, i.e., Yb^{3+}, into lead-free double perovskite $Cs_2AgBi(Cl/Br)_6$ PNCs, generating a dual-color emission with their intrinsic trap-related visible emission centered at about 680 nm and a newly emerged NIR emission band centered at about 1000 nm, respectively.[88] The emission tunability toward

Table 1. Summary of the dual-color emission properties of variable PNCs with different cation dopants.

Dopant	Host PNCs	Doping amount [atom%]	PL_{BE} peak [nm]a)	PL_{Dop} peak [nm]	Temp [K]b)	PLQY [%]	τ_{BE} [ns]c)	τ_{Dop} [ms]	Ref.
Mn^{2+}	$CsPbCl_3$	1–8%	402	585	293	27	–	1.4	[236]
Mn^{2+}	$CsPbCl_3$	0.8–11.2%	402	602	293	–	0.4	1.5	[70]
Mn^{2+}	$CsPbCl_3$	1–40%	398–414	579–592	80–350	5–35	8.8–14.9	1.21–1.33	[71]
Mn^{2+}	$CsPbCl_3$	0.3–0.7%	402–414	590–605	10–300	16.9–46.9	0.47–3.38	0.0075–1.26	[72]
Mn^{2+}	$CsPbCl_{3-x}Br_x$	2.80%	403–442	593–601	4.2–300	4–60	0.5–12.6	–	[73]
Mn^{2+}	$CsPbCl_{3-x}Br_x$	65%	420–517	600	293	3.5–51.9	13–28.6	0.46–0.89	[74]
Mn^{2+}	$CsPbCl_{3-x}Br_x$	2%	≈400	610–625	293	–	–	0.3–1	[75]
Mn^{2+}	$CsPbX_3$ (X = Cl, Br and I)	Cl: 3.5–7.6%, Br: 2–6.2%, I: 3.2–39.3%	404 ($CsPbCl_3$)	600	77–473	Cl: 12.7, Br: 57.1, I: 89.6	3.2–5 (Cl)	1.2 (Cl:Mn)	[68]
Mn^{2+}	$CsPbI_3$	10%	680	680	293	74–82	14	17 ns	[77]
Mn^{2+}	$CsPb(Cl/Br)_3$ dispersed glass	–	520	600	293	40	122	2.85	[78]
Mn^{2+}	$(PEA)_2PbBr_4$	39–53%	412–420	595–600	77–300	9.4–45	–	–	[79]
Mn^{2+} and Ni^{2+}	$CsPbCl_3$	Mn^{2+}: 0.53–18.09%, Ni^{2+}: 0–19.05%	398–405	599–638	80–300	5–70	–	1.01–1.80	[80]
Sn^{2+}, Zn^{2+}, and Cd^{2+}	$CsPbBr_3$	Sn^{2+}: 0.2%, Cd^{2+}:0.5%, Zn^{2+}: 0.7%	512	Sn^{2+}: 479–506, Zn^{2+}: 452–483, Cd^{2+}: 462–505	293	43–62	16.8	Sn^{2+}: 6.8–10.6 ns, Zn^{2+}: 7.2–15.2 ns, Cd^{2+}: 6.4–8.1 ns	[81]
Bi^{3+}	$CsPbBr_3$	0.25–2.1%	517	512	293	8–78	7	4.5–5.2 ns	[82]
Eu^{3+} and Tb^{3+}	$CsPbBr_3$	Eu^{3+}: 4.60%, Tb^{3+}: 3.03%	541–543	Eu^{3+}:592 and 612, Tb^{3+}: 582 and 617	293	–	3.8	Eu^{3+}: 0.37, Tb^{3+}: 1.63	[86]
Ce^{3+}	$CsPbBr_3$	0.43–2.88%	516	510	293	41–89	18.3	1.27 ns	[87]
Yb^{3+}	$Cs_2AgBi(Cl/Br)_6$	0.5–5.5%	680	1000	293	0.30	5.7–33.4	0.97–1.44	[88]

a)BE emission peak; b)Characterization temperature; c)Lifetime of BE emission.

the NIR regime induced by the doping effect will be reviewed in detail in Section 4. We have highlighted the key characteristics of the dual-color emission from the most representative reported works related to halide PNCs in **Table 1**.

In summary, doping engineering is a powerful approach to tune and stabilize the PL properties of halide PNC hosts via energy transfer mechanisms that lead to enhanced dopant emission. There is a trade-off issue for the optimization of dual-color emission induced by doping. The doping amount needs to be optimized to positively affect the PLQY of the host PNCs by surface passivation by the dopant cations and the simultaneous additional emission from the dopants themselves. At high dopant (e.g., Mn) concentrations, there is a potential to observe strong Mn^{2+}–Mn^{2+} interactions, resulting in a sharp reduction of the Mn^{2+}-related PLQY due to the formation of the defects in the mid bandgap of the host PNCs induced by the excess of Mn doping.[89] These formed small Mn^{2+} clusters can increase the number of electron traps leading to an energy loss in the form of nonradiative recombination. Therefore, it is undoubtedly urgent to thoroughly investigate the doping-induced lattice rearrangement and the resultant effect on the PL (excitonic) properties with more research efforts.

5. Broadly Tunable Emission Toward NIR

Together with the extensive efforts made to fine-tune the PL properties of PNCs in the range of UV-to-visible, researchers have also actively investigated the possibility to extend the use of PNCs up to the NIR spectral region, which is known to lack highly efficient and stable emitters. In fact, such emitters find utilization in a large number of applications, such as optical bioimaging in the biological NIR optical window (650–900 nm),[90–92] infrared detectors for optical communication (wavelengths around 1.3 and 1.55 μm due to the lowest chromatic dispersion and optical losses) and night vision systems (0.7–1.0 μm),[93,94] chemical identification and imaging in the whole NIR region,[95] and the improvement of photovoltaic devices by expanding the spectral range of their sensitivity[96] or through quantum-cutting effect.[97] This has led to an increased interest in NIR-emitting perovskites and corresponding devices.[98] The most intensively studied and well-established PNCs have the PL band in the visible spectral region that limits their use in a variety of photonic and optoelectronic applications. This problem requires searching for new strategies for PNC synthesis to extend the PL bands to longer wavelengths, i.e., in the NIR range. The recently developed approaches may be mainly

divided into several categories, namely stoichiometry control, doping, and heterostructuring.

The structure of perovskites allows great flexibility in tuning their composition with several chemical elements to obtain a wide range of optoelectronic materials. Each of these materials has distinctive features, and both the position of the PL band and the stability of the material vary greatly with the stoichiometry. For some compositions, the PL band can be pushed to the NIR (**Figure 4**a). The PL window of the well-studied $MAPbI_3$ composition is in the range of 730–750 nm.[99,100] The $FAPbI_3$ composition attracted attention due to the possibility to both obtain more stable PNCs while simultaneously extending the PL band to the NIR spectral region. Ultrasonic synthesis of $FAPbI_3$ PNCs was demonstrated by Jang et al.[100] The 10 nm PNCs obtained by this method displayed

strong emission at 805 nm with a PLQY of 78%. Levchuk et al. reported the ligand-assisted reprecipitation (LARP) synthesis of $FAPbX_3$ PNCs, in 2017.[101] When X = I, the nanocrystals had a cubic shape with a size of 14.4 ± 3.4 nm, and their PL was centered at 740 nm. In addition to the high PLQY (55%) and a narrow emission band, the obtained PNCs demonstrated superior stability as compared with their MA-based counterparts. Thus, it was demonstrated that PNCs may possess strong and narrow emission close to the NIR spectral region. It should be pointed out that the emission positions for $FAPbI_3$ PNCs reported by different groups vary in a quite broad range, which may be attributed to both different synthetic methods and conditions and variation of PNCs size.[102]

Protesescu et al. used two- and three-precursor approaches to synthesize $FAPbI_3$ PNCs by a hot-injection method.[103] Both
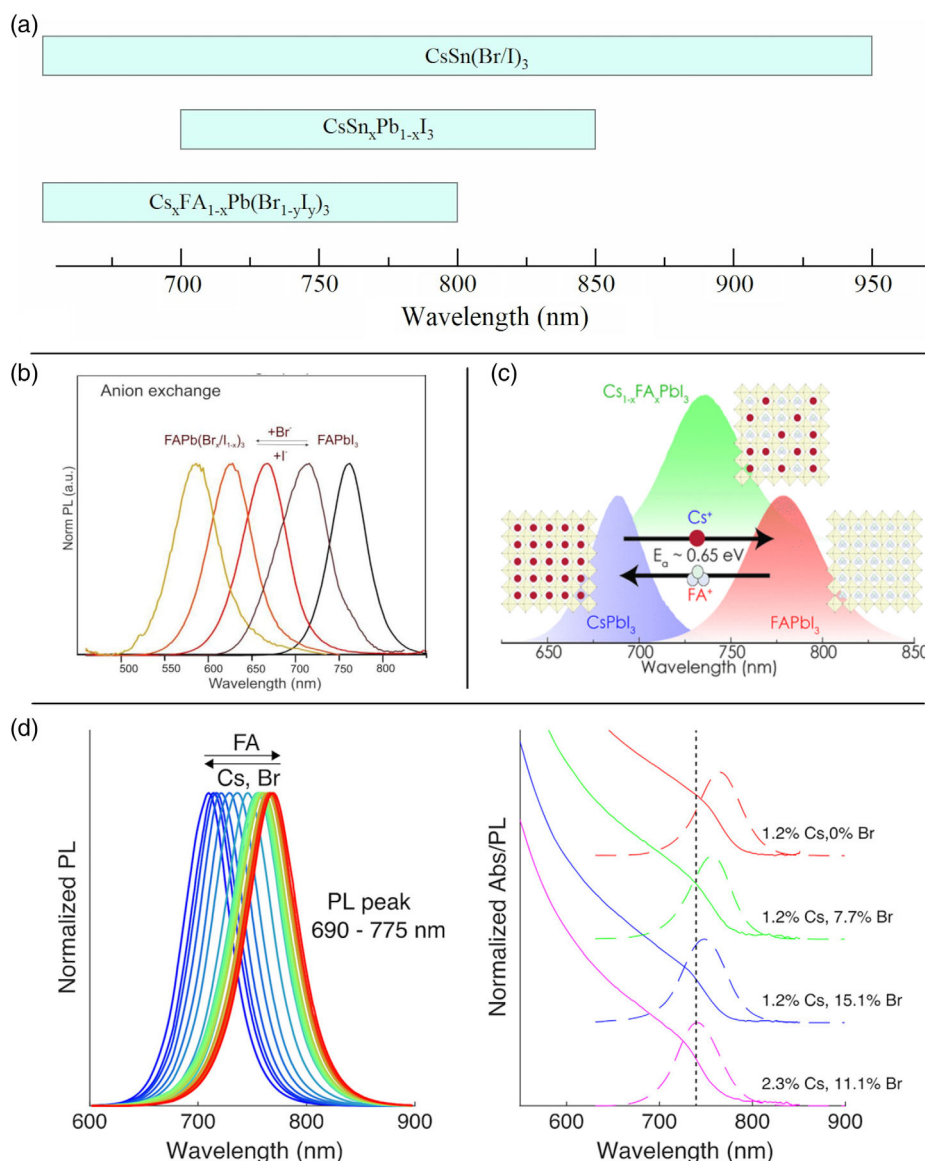

Figure 4. a) The tuning of the PL from organic–inorganic and all-inorganic PNCs in the NIR. b) Anion and c) cation exchange with $FAPbI_3$ PNCs for PL band tuning. b) Reproduced with permission.[103] Copyright 2017, American Chemical Society; c) Reproduced with permission.[109] Copyright 2018, American Chemical Society. d) Tuning the PL position in multinary $Cs_xFA_{1-x}Pb(Br_{1-y}I_y)_3$ PNCs. Reproduced with permission.[111] Copyright 2018, American Chemical Society.

approaches allowed achieving nearly cubic PNCs with a size of 10–12 nm. The intense (PLQY > 70%) PL band with a width of 45 nm was centered at 770–780 nm. Importantly, the PLQY remained extremely high even after several months of storage. For application in light-emitting devices, an important characteristic is the preservation of a high PLQY (>20%) after PNCs washing and annealing of their thin films at 100 °C. The authors demonstrated the possibility of cation (Cs^+ to FA^+ and vice versa using FA- and Cs-oleates, respectively) and anion (I^- to Br^- using oleylamine (OAm^+)Br^-) exchanges. This postsynthetic procedure is a versatile tool to tune the PL position of $FAPbI_3$ PNCs with the preservation of a high PLQY and narrow PL bandwidth (Figure 4b). High stability and PLQY allowed the creation of a LED with an indium tin oxide (ITO)/poly(3,4-ethylenedioxythiophene) polystyrene sulfonate (PEDOT-PSS)/$FAPbI_3$/TPBi/LiF/Al structure. The LED displayed a NIR emission at 772 nm with an external quantum efficiency (EQE) of 2.3%. An additional benefit of cation and anion exchange procedures is related to the structural aspects of PNCs. It is known that the phase stability of PNCs is directly associated to the nature of the perovskite material.[104] The adjustment of perovskite composition allows not only PL band tuning but also the improvement of tolerance factor and phase stability. Thus, a thorough fine-tuning or/and exchange of cations[105] and anions[106] impact both luminescent and structural properties. For instance, it was shown that some mixed halide combinations demonstrate superior ambient stability,[107] which is also valid for mixed cation combinations.[108]

Later, Hazarika et al. demonstrated cation exchange between $CsPbI_3$ and $FAPbI_3$ nanocrystals to obtain a full gamut of $Cs_{1-x}FA_xPbI_3$ PNCs with a tunable PL from 650 to 800 nm (Figure 4c).[109] Being mixed at different concentrations, PNCs were able to form a desired Cs/FA stoichiometry. The kinetics of the process was studied by PL spectroscopy: at the initial stage, PL spectra showed two distinct PL bands that then merged, and bimodal PL spectra were observed until the reaction was not completed. The heating of the PNCs mixture accelerated the cation exchange process. The carrying out of the reaction at different temperatures allowed estimating the activation energy of the exchange process, which turned out to be significantly higher than the values previously reported for the exchange of halogens. The proposed postsynthetic cation exchange method is the only effective one for obtaining the Cs/FA alloyed perovskites. Begum et al. have recently demonstrated that doping of $FAPbI_3$ PNCs by Sn^{2+} provides a slight increase in the perovskite bandgap and the PL peak position shifts from 797 nm for pristine 12.5 nm $FAPbI_3$ PNCs to 775 nm for the PNCs with 2.44% of Sn^{2+}.[110] At the same time, the Sn^{2+} doping allowed a significant increase in the PLQY which can be attributed to the reduced formation of traps and suppressed Auger recombination.

The use of multinary compositions (mixed cation and anion) promotes achieving even more precise tuning of the PL band position. Lignos et al. showed that the addition of Br^- into $CsFAPbI_3$ PNCs leads to the formation of more chemically and thermodynamically stable PNCs.[111] They used a special microfluidic platform, which is an ideal instrument for systematic variation of precursors and investigation of PNCs of different stoichiometry. While the variation of FA/Pb and Cs/Pb molar ratios allows tuning the PL band in the 690–780 nm region, the insertion of Br^- also leads to an additional blue shift of the PL peak position (Figure 4d).

The authors used $Cs_xFA_{1-x}Pb(Br_{1-y}I_y)_3$ PNCs to fabricate LEDs emitting at ≈730 nm with the EQE as high as 5.9%. The use of additional cyclic olefin copolymer allowed to achieve the extra narrow EL band of 27 nm.

All-inorganic cesium lead halide PNCs attracted much attention due to the improved thermal stability.[8,112] At the same time, they keep all the key advantages of hybrid organic–inorganic PNCs, such as excellent optical properties, tunability, and high carrier mobility. Hence, they can become a promising new platform for novel optoelectronic devices.[113] However, their emission is limited at ≈690 nm for the $CsPbI_3$ composition. Fortunately, their PL band can be tuned further to the NIR when part of Pb^{2+} is replaced by Sn^{2+}. From a structural point of view, doping of $CsPbI_3$ PNCs with smaller cations should lead to better phase and thermal stability due to the partly reduced bond length.

Liu et al. used SnI_2/PbI_2 mixture with different ratios during hot-injection PNCs synthesis to obtain 11–14 nm $CsSn_{1-x}Pb_xI_3$ PNCs.[114] Partial replacement of Pb^{2+} by Sn^{2+} allowed to push the emission band into the NIR (**Figure 5**a). The downside of creating such alloyed nanocrystals is a critical decrease in the PLQY, which was only 0.3–3% for the PNCs upon different stoichiometry. Such a reduction of PLQY is attributed to the formation of intrinsic defects related to Sn vacancies with low formation energy.[115] On the other hand, the alloyed PNCs demonstrated superior environmental stability (over 5 months in air) as compared with the pure $CsSnI_3$ PNCs (Figure 5c), which are an extreme case of NIR-emitting inorganic perovskite NCs.[116] Liu et al. have recently demonstrated the possibility to drastically enhance the PLQY of alloyed $CsSn_{1-x}Pb_xI_3$ PNCs by Na doping.[117] The very small fraction of Na helps to stabilize Sn^{2+}, and the optimized PLQY reached 28%. Lead-free nontoxic $CsSnI_3$ inorganic PNCs are a very attractive class of NIR emitting nanomaterials with a PL band at ≈900–950 for the 0D form and ≈780 nm for the 2D nanoplates.[118] For the first time, Jellicoe et al. demonstrated the synthesis of $CsSnX_3$ (X = Cl, Br, I) and the possibility to obtain their intermediate compositions using both direct synthesis and postsynthetic anion exchange (Figure 5b).[116] The most significant drawbacks of these nanocrystals are the very low PLQY and poor stability. For the development of NIR photonics based on perovskite nanomaterials, it is rather necessary to solve the indicated problems. At present, several approaches, including a search of optimal precursors, stoichiometries, dopants, and additives, are considered.[119–121] The creation of nontoxic, inexpensive, efficient, and stable NIR-emitting PNCs is accordingly an important and urgent task.

Two other approaches to achieve NIR emission from perovskite PNCs, namely doping and heterostructuring, assume the use of emission from different species embedded into a PNC matrix. Thanks to the large absorption cross-section, high PLQY, and octahedral coordination environment of perovskite-based compounds, PNCs can be considered as a new and prospective host for the doping with lanthanides. In contrast to most semiconductors, a coordination number of 6 is preferred for successful doping with lanthanides.[122] Being introduced into a PNCs, lanthanides do not demonstrate their own absorption band but are photosensitized by the perovskite host, and such lanthanide-doped PNCs demonstrate multiple emission peaks. An appropriate choice of lanthanide precursors allows the achieving of a variety of doped $CsPbCl_3$ and $CsPbCl_xBr_{1-x}$ PNCs by a
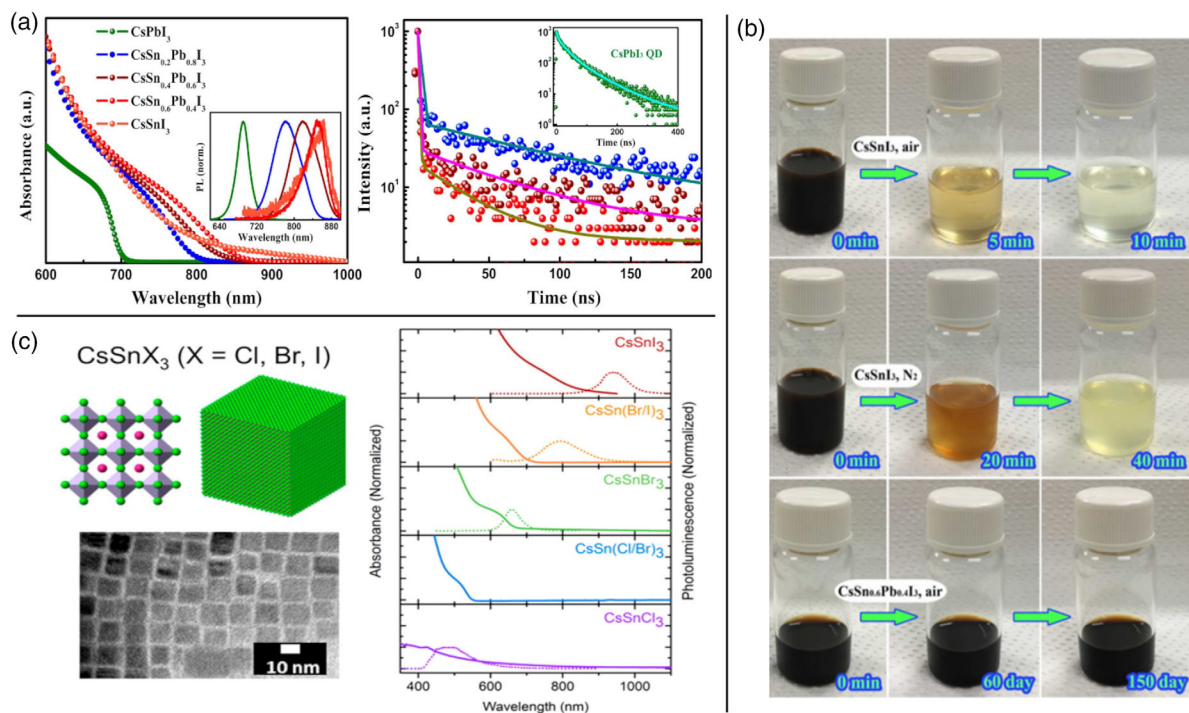
Figure 5. a) Absorption and PL spectra and PL decay curves obtained for $CsSn_{1-x}Pb_xI_3$ NCs. Reproduced with permission.[114] Copyright 2017, American Chemical Society. b) The comparison of the stability of Sn-based and alloyed $Sn_{1-x}Pb_x$-based all-inorganic perovskite NCs. Reproduced with permission.[114] Copyright 2017, American Chemical Society. c) The schematic and TEM images, absorption, and PL spectra for nontoxic Sn-based perovskite NCs with different halogens. Reproduced with permission.[116] Copyright 2016, American Chemical Society.

direct hot-injection synthesis,[123] whereas postsynthetic treatment[124] and anion exchange[125] are more suitable when $CsPbBr_3$ or $CsPbI_3$ PNCs are selected as the host.

The first doping of $CsPbCl_xBr_{1-x}$ PNCs with Yb^{3+}, Ce^{3+}, and Er^{3+} atoms was reported by Zhou et al. (as mentioned in Section 3), who designed these PNCs to improve the performance of commercial silicon solar cells by downconverting the UV and deep-blue emission.[85] Due to the quantum cutting effect, the PLQY exceeded 100% and reached 146% for the $CsPbCl_{1.5}Br_{1.5}$:Yb(7.1%),Ce(2%) composition. The quantum cutting effect becomes possible when a material absorbs a photon with an energy more than twice larger than it emits. In this case, the high-energy absorbed photon can be converted into two photons with lower energy.[126,127] The most intense NIR emission originates from the $^2F_{5/2}$–$^2F_{7/2}$ transition in the Yb^{3+} ions and is excited by the PNC host, as can be monitored by a strong reduction of the excitonic emission lifetime. An additional weak NIR emission in codoped PNCs is centered at 1540 nm and originates from Er^{3+} ions (**Figure 6**a). Er^{3+} ions were nonradiatively excited by Yb^{3+} ions and not by the PNC host, which was accompanied by the reduction of Yb^{3+}-related PL lifetime. Zhang et al. also observed Er^{3+}-related emission only for Yb^{3+}, Er^{3+} codoped $CsPbCl_3$ PNCs.[128] Milstein et al. further investigated the quantum cutting effect in Yb^{3+}-doped $CsPb(Cl_{1-x}Br_x)_3$ PNCs in more detail.[125] Using the anion exchange reaction, they obtained a number of PNC stoichiometries to determine the absorption band threshold position for quantum cutting. They showed that a bandgap can be narrowed down to 2.53 eV while still retaining a

PLQY higher than 100%. Below this threshold, the excitation energy is not high enough to realize the quantum cutting regime. It should be noted that such NIR-emitting colloidal PNCs with large Stokes shift and high PLQY are also very promising for solar concentrator applications.[122,129] In addition to demonstrating their own NIR emission, lanthanide ions can improve the optical and electrical properties of the perovskite host. Yb^{3+}-doped $CsPbI_3$ PNCs demonstrated a reduced trap-state density, and, as a result, higher PLQY and better charge carrier transport compared with the case without Yb^{3+}-doping.[130]

$A_2B^IB^{III}X_6$ double perovskites, where two divalent Pb^{2+} ions are replaced by one monovalent and one trivalent metal ions (B^I, B^{III}), are an important class of lead-free perovskite nano- and micromaterials. Being lead-free and intrinsically stable, double perovskite PNCs are intriguing materials that can host several ion dopants.[121,122] Nag and coworkers have recently reported the hot-injection synthesis of Yb^{3+}-doped $Cs_2AgInCl_6$ PNCs using $Yb(NO_3)_2 \cdot 5H_2O$ as Yb^{3+} precursor.[131] The use of a high concentration of $Yb(NO_3)_2 \cdot 5H_2O$ precursor (more than 50%) yielded only 6.2% of Yb^{3+} inside the synthesized PNCs, indicating difficult insertion of this lanthanide ion into the $Cs_2AgInCl_6$ matrix. The same observation was reported by Kim and coworkers, who pointed out that only a small portion of Yb^{3+} can be inserted into a $Cs_2AgInCl_6$ matrix, whereas a larger amount of Yb^{3+} containing precursor can induce a formation of undesired secondary phases.[132] Similarly to the $CsPbX_3$ PNCs, the NIR PL centered at 996 nm is excited through the perovskite matrix. But in contrast to the case of $CsPbX_3$,[85,128]
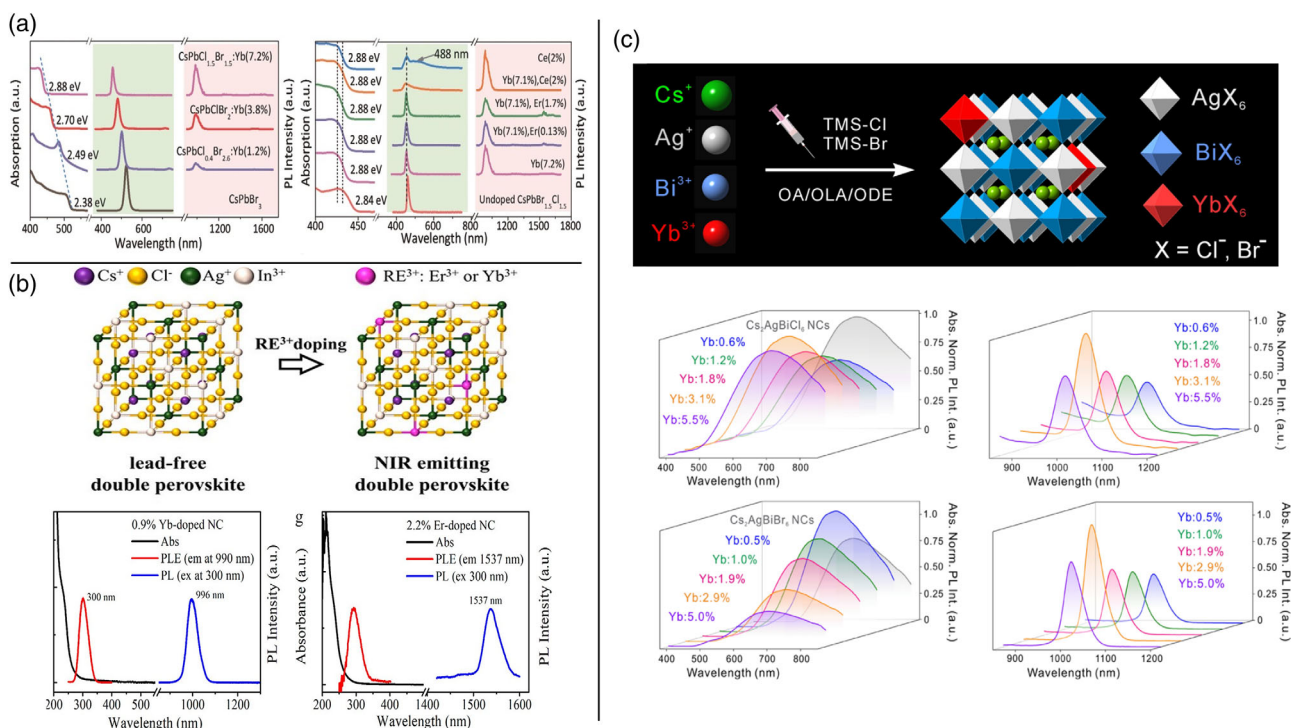
**ADVANCED
SCIENCE NEWS**

www.advancedsciencenews.com

**ADVANCED
PHOTONICS
RESEARCH**
Open Access

www.adpr-journal.com

Figure 6. The doping of inorganic PNCs with lanthanides. a) The PL spectra of $CsPbCl_xBr_{1-x}$ PNCs doped with Yb^{3+}, Ce^{3+}, and Er^{3+} atoms. Reproduced with permission.[85] Copyright 2017, Wiley-VCH. The structure and PL spectra of doped b) $Cs_2AgInCl_6$ and c) $Cs_2AgBiCl_6$ (X = Cl, Br) double PNCs. b) Reproduced with permission.[132] Copyright 2019, American Chemical Society. c) Reproduced with permission.[88] Copyright 2019, American Chemical Society.

Er^{3+}-related emission in $Cs_2AgInCl_6$ PNCs can be directly excited by the nonradiative energy transfer from the perovskite host, eliminating the need for Yb^{3+}, Er^{3+} codoping (Figure 6b).[132] However, it was shown that codoping still can enhance the NIR emission from Er^{3+} centers. Nag and coworkers applied Bi^{3+}, Er^{3+} codoping for $Cs_2AgInCl_6$ double PNCs. They showed that, after the Bi^{3+} doping, the new absorption band centered at 372 nm appears for both only Bi^{3+} and Bi^{3+}, Er^{3+} codoped samples, in turn allowing their excitation using commercially available UV LED chips. In this way, Bi^{3+} dopants reduce the required excitation energy and transfer the excitation to the visible and NIR emissive states. In other words, Bi^{3+} dopants act as sensitizing centers for the Er^{3+}-related NIR emission that leads to both intensity enhancement and decay slowdown of the NIR PL.[133] The doping by NIR-emitting Yb^{3+} lanthanide was extended for different double halide perovskite compositions. Chen et al. studied the doping of $Cs_2AgBiCl_6$ (X = Cl, Br) PNCs with Yb^{3+} and Mn^{2+} ions (Figure 6c).[88] They showed that the increase in Yb^{3+} concentration in a moderate range provides the enhancement of both excitonic and NIR PL, which can be attributed to the passivation of trap states and increase in the emitters number, respectively. However, at a larger concentration, both PL signals became weak because of the concentration quenching effect. This effect is a well-known for luminescent dopants, including lanthanides, in various matrixes. The concentration quenching is also typical for PNCs with a high degree of doping.[134–136] In most cases, the quenching occurs upon the excitation migration between closely located dopants. As a result, the excitation may be nonradiatively transferred into a nonemissive site.[137,138] Despite the promising initial results achieved with these systems and their huge potential, the NIR PLQY does not exceed several percent for the Yb^{3+} centers, and it is even about one order of magnitude smaller for the Er^{3+} centers. Obviously, much effort is still required to make the properties of these PNCs suitable for optoelectronic applications.

Engineering of nanocrystal heterostructures based on perovskite platform is a novel concept to achieve optoelectronic materials with synergetically improved characteristics.[139] Heterostructures made of all-inorganic PNCs and lead sulfide (PbS) QDs provide a unique opportunity to utilize the strong PL in the NIR from QDs far inside the matrix of the nanosized perovskite material. Zhang et al. have recently reported the RT synthesis of heterostructured $CsPbX_3$–PbS PNCs with a dual emission.[140] $CsPbCl_3$–PbS were formed by chemical reaction of presynthesized pristine PNCs with bis(trimethylsilyl)sulfide ($(TMS)_2S$) precursor. The $CsPbBr_3$–PbS and $CsPbI_3$–PbS PNCs can be obtained by either analogical postsynthesis with $(TMS)_2S$ or anion exchange using $PbBr_2$ or PbI_2, respectively, in a mixture of 1-octadecene (ODE), oleic acid (OA), and oleylamine (OLA) (**Figure 7**). The growth of PbS QDs inside the heterostructured PNC is realized by the partial transformation of an initial perovskite QD to PbS QDs by means of interaction with $(TMS)_2S$. The optimal time of reaction for the coordination between PNCs and PbS QDs allows achieving the highest PLQY in both visible and NIR spectral regions. The system enables further tuning of both emission bands by varying
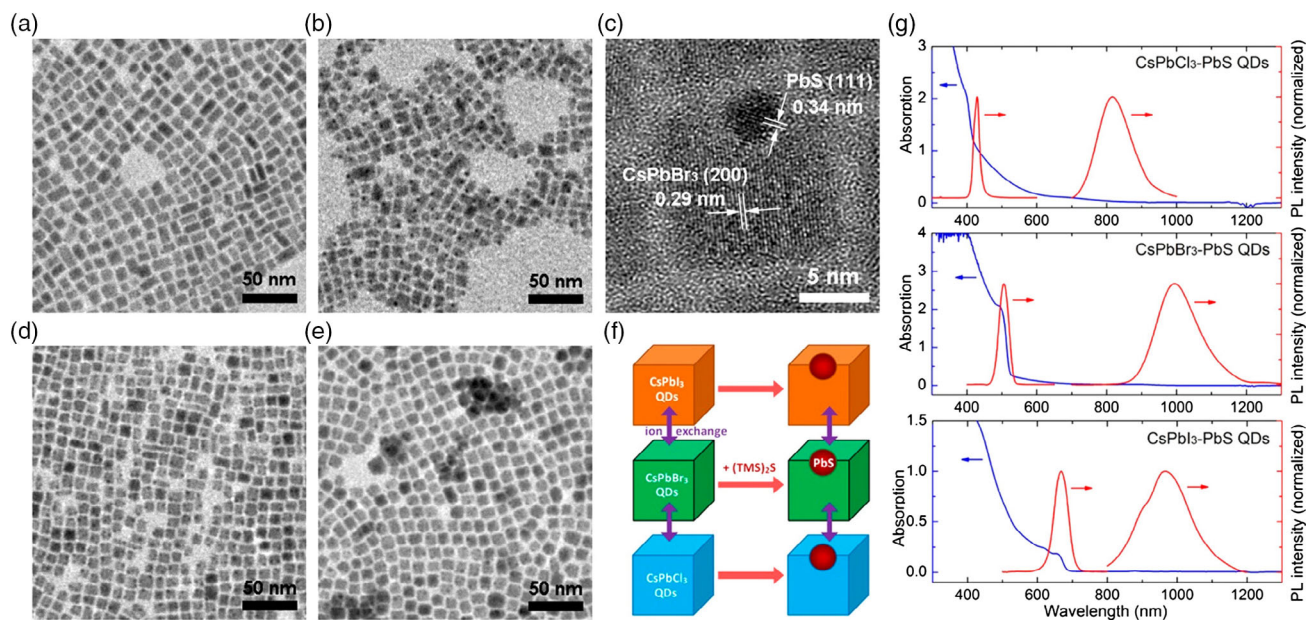
Figure 7. Heterostructuring with $CsPbX_3$ PNCs for obtaining the dual emission. a) TEM images of the original $CsPbBr_3$ pNCs, b,c) TEM and high resolution TEM (HRTEM) images of $CsPbBr_3$–PbS PNCs, TEM images of d) $CsPbCl_3$ and e) $CsPbI_3$ PNCs; f) the schematic of the heterostructures fabrication and g) corresponding absorption and PL spectra. Reproduced with permission.[140] Copyright 2020, American Chemical Society.

the perovskite stoichiometry, time of reaction, and $(TMS)_2S$ amount.

6. Emission Thermal Quenching

The temperature of the environment has been also widely acknowledged as a key factor that influences both crystals structures and band structures of halide PNCs, resulting in a change in the PL properties. In general, the emission intensity of luminescent materials progressively decreases with increasing temperature, and this phenomenon is known as emission thermal quenching (TQ).[141] Backlit displays for LCD applications typically operate at 40–50 °C,[142] and the operating temperature can reach as high as 200 °C in the case of high-power phosphor-converted LEDs.[141] Therefore, emission TQ is one of the crucial phenomena that strongly affects the performance of luminescent materials toward various luminescence-based applications. Materials with a robust crystal structure, such as rigid inorganic phosphors, exhibit a low-emission TQ intensity.[141]

Debye temperature is a reliable parameter for structural rigidity: a high value indicates a more rigid structure.[143] PNCs possess a soft crystal structure, in agreement with their relatively low Debye temperature ($\approx$300 K).[144] At elevated temperatures, PNCs experience strong emission quenching. Schaller and coworkers have systematically studied the temperature-dependent emission properties of $CsPbX_3$ (X = Cl, Br, and I) PNCs.[144] All the PNCs exhibited reversible emission intensity quenching up to a temperature of 400–450 K. The reversible emission loss has been attributed to the heat-induced charge-carrier trapping by the halogen vacancies.[144,145] Furthermore, Woo et al. systematically studied how the emission intensity of $MAPbBr_3$ PNCs would be comparable with that of $MAPbBr_3$ thin films and single

crystals when increasing the temperature from 20 to 300 K (**Figure 8**a).[146] All three $MAPbBr_3$ samples (PNCs, thin films, single crystals) exhibited a drop in their PL intensity when increasing the temperature. However, the emission decay is much slower in the case of PNCs because of their higher exciton binding energy (388.2 meV) compared with thin films (124.3 meV) and single crystals (40.3 meV). The low exciton binding energy facilitates easier thermal dissociation of loosely bound charge carriers in the case of $MAPbBr_3$ thin films and single crystals. On the other hand, phonon-assisted thermal escape of the charge carriers is attributed to the primary nonradiative decay pathway of the exciton with increasing temperature in the case of $MAPbBr_3$ PNCs. The optical phonon energies of $MAPbBr_3$ PNCs, thin films, and single crystals were measured to be $\approx$25, 31, and 53 meV, respectively. Such lower phonon energy indicates that the scattering of the charge carriers by the phonons is higher in the PNCs than in thin films and single crystals. The exciton-phonon coupling, which serves as the exciton's nonradiative decay pathway in $MAPbBr_3$ PNCs, becomes prominent at elevated temperatures, resulting in PL intensity loss. Fang et al. studied the emission TQ behavior of $FAPbI_3$ (FA = formamidinium) PNCs and thin films in the 20–300 K regime.[147] The emission quenching properties in a low-temperature regime shed light on the basics of halide perovskite emission properties. The $FAPbI_3$ PNC ensemble exhibited negative emission TQ behavior, which corresponds to a rise in the emission intensity with increasing temperature. At higher temperatures, the increase in the emission intensity is attributed to the activation of charge carriers trapped at the surface of PNCs, which radiatively recombine, in turn contributing toward the emission intensity enhancement. On the contrary, polycrystalline films of $FAPbI_3$ exhibited strong emission TQ, resulting
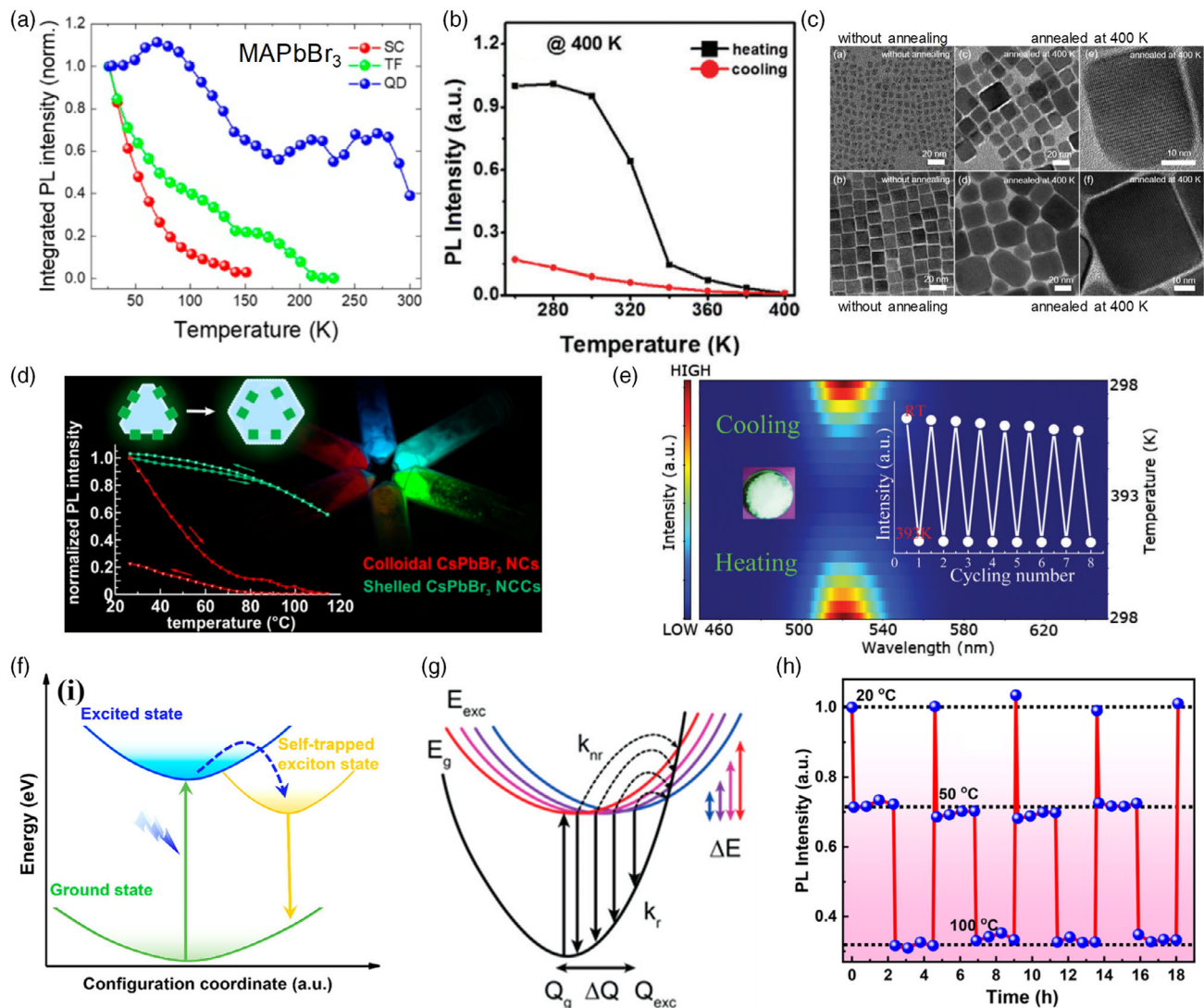
Figure 8. a) Integrated PL intensity variation of MAPbBr$_3$ PNCs, thin film, and single crystals as a function of temperature. Reproduced with permission.[146] Copyright 2018, American Chemical Society. b) Integrated PL intensity variation of CsPbBr$_3$ PNC films as a function of temperature up to 400 K, followed by cooling back to RT. Reproduced with permission.[145] Copyright 2017, The Royal Society of Chemistry. c) Low- and high-resolution TEM images of two different sizes of CsPbBr$_3$ PNCs before (left) and after (middle and right) thermal annealing at 400 K for 20 min. Reproduced with permission.[145] Copyright 2017, The Royal Society of Chemistry. d) Heating–cooling cycles of bare and NaBr-coated green-emitting PNCs. Reproduced with permission.[142] Copyright 2019, American Chemical Society. e) Heating–cooling cycles of CsPbBr$_3$ PNCs embedded in a Cs$_4$PbBr$_6$ matrix. Reproduced with permission.[152] Copyright 2016, The Royal Society of Chemistry. f) Configuration coordinate energy diagram depicting the exciton self-trapping and STE emission mechanism in lead-free PNCs. Reproduced with permission.[159] Copyright 2020, American Chemical Society. g) Single-coordinate energy diagram illustrating the nonradiative (k_{nr}) exciton recombination pathway related to STE emission with varying activation energies and, hence, with varying Stokes shift. Reproduced with permission.[158] Copyright 2020, American Chemical Society. h) Integrated PL intensity variation of Cs$_3$Cu$_2$I$_5$ PNCs during heating–cooling cycles. Reproduced with permission.[159] Copyright 2020, American Chemical Society.

from both thermal dissociation of charge carriers (due to lower exciton binding energy) and trap-mediated nonradiative recombination. Furthermore, FASnI$_3$ single crystals and thin films also exhibit negative emission TQ behavior—the PL intensity initially increases upon cooling down the samples from RT, with a maximum in the intensity at 185 K, and with additional decrease upon further cooling. The negative emission TQ behavior originates from the phase transitions that take place upon the cooling of FASnI$_3$.[148] Whether such phase transition behavior exists or

not in their corresponding nanocrystal form can be demonstrated by studying the emission TQ behavior of FASnI$_3$ PNCs. The negative emission TQ in the low-temperature regime was also detected in a white-light-emitting low-dimensional lead halide perovskite.[149]

Thermogravimetric analysis showed that very high temperatures (above 400–450 K) can generate enough heat to detach the ligands from the surface of PNCs. This, in turn, promotes the PNC agglomeration, followed by an irreversible emission

**ADVANCED
SCIENCE NEWS**

www.advancedsciencenews.com

**ADVANCED
PHOTONICS
RESEARCH**
Open Access

www.adpr-journal.com

decay (Figure 8b).[144,145] Figure 8c shows that $CsPbBr_3$ PNCs agglomerate (and hence there is a loss of quantum confinement) via the ripening process upon thermal annealing at 400 K. Also, $CsPbCl_3$ and $CsPbBr_3$ PNCs experience the highest- and lowest-emission TQ among $CsPbX_3$ PNCs, suggesting the halide-composition dependency of emission TQ behavior in PNCs. The broadness of the PL spectra increases as a function of temperature, and the broadness is higher compared with conventional II-VI semiconductor NCs at a given temperature, arising from a complex longitudinal optical phonon-exciton coupling.[144]

It is imperative to preserve the emission properties of PNCs at elevated temperatures for their practical applications. Embedding or encapsulating them in a matrix has been proven to be a successful strategy for reducing emission TQ. Wang et al. demonstrated that mesoporous silica–$CsPbBr_3$ PNC composites exhibited improved thermal stability compared with bare $CsPbBr_3$ PNCs, retaining 40% of initial PL intensity when being heated up to 100 °C.[150] Also, the PL intensity of the nanocomposite fully recovered upon cooling it back to RT. Alumina coating also improved the emission stability of $CsPbBr_3$ PNC films at high temperatures.[151] Recently, Kovalenko and coworkers have demonstrated that the emission thermal stability of the PNCs increases substantially with negligible variation in the PL maximum energy upon encapsulating them in an inorganic microcrystal.[142] Green-emitting PNC/NaBr core–shells did not display any drop in their PLQY at 40–50 °C, with 60% and 70% of initial PL intensity retained at 100 and 120 °C, respectively (Figure 8d). Notably, about 60–70% of the initial PLQY was recovered even upon annealing the microcrystal-shelled lead halide PNCs at 80 °C for 190 h, which demonstrates the high potential of this PNC-composite in LED applications. The emission properties of the green-emitting $CsPbBr_3$ PNCs remained unaffected by the thermal annealing process when they are embedded inside a Cs_4PbBr_6 matrix.[152,153] The PL intensity almost reverted to the initial value when cooling the sample to RT from 120 °C, and the process was reproducible for several heating–cooling cycles (Figure 8e).[152] Similarly, brightly red-emitting $CsPbI_3$–Cs_4PbI_6 hybrid PNCs preserved nearly 65% and 60% of their initial PLQY at 150 °C and after thermal annealing at 100 °C for 6 h, respectively.[154] In the PNC–matrix composites, the individual PNCs are spatially separated from each other by the matrix, which prevents the PNC agglomeration under the continuous thermal annealing and hence preserves the emission properties of the PNCs.

In the case of lead-free PNCs and their bulk counterparts, the emission process occurs via exciton self-trapping.[155,156] A high electron-phonon coupling in these materials produces a STE state as an additional excited state. The photogenerated charge carriers are self-trapped from the free energy state to the lower energy (stable) STE state, followed by the radiative recombination to produce the STE emission (Figure 8f).[157] Thermal-annealing quenches the STE emission intensity via the STE detrapping, followed by nonradiative relaxation to the ground state.[156] The detrapping process has an activation barrier and, hence, can be accelerated with the increasing temperature (Figure 8g).[158] For instance, the PL intensity of $Cs_3Cu_2I_5$ PNCs increasingly quenches as a function of temperature via the STE detrapping, similar to the case of bulk $Cs_3Cu_2I_5$ (Figure 8h).[157,159] On the other hand, the STE emission of $Cs_3Cu_2I_5$ increases as a function

of temperature in the low-temperature regime via thermal-assisted STE emission enhancement.[160] Also, it is interesting to note that $Cs_3Cu_2Cl_5$ exhibits substantially higher emission stability compared with $Cs_3Cu_2Br_5$ and $Cs_3Cu_2I_5$.[161] High exciton binding energy, low energy transfer, and strong Cu—Cl bond were proposed as the possible causes of the lower-emission TQ observed in the case of $Cs_3Cu_2Cl_5$.

7. PNC-based LED Applications

7.1. Lead-based PeLEDs

Metal halide PNC-based LEDs (PeLEDs) have recently gained significant interest due to their low-cost solution processability, bright luminescence, good mass-production yield, and size- and composition-dependent light emission from violet to NIR regions.[162–167] The already mentioned near-unity PLQYs, excellent color purities, and easily tunable emission energies with very narrow bandwidths (typically referred to as full-width at half-maximum [FWHM] bandwidth) of PNCs make them potential candidates for high-quality lightings, displays, and optical communications.[168–170] Organic–inorganic (e.g., $FAPbBr_3$, $MAPbBr_3$) PNCs,[171–173] 2D perovskites (e.g., $PBABr(C_6H_5(CH_2)_4NH_3Br)$, $PBA_2(CsPbBr_3)_{n-1}PbBr_4$),[174,175] all-inorganic ($CsPbX_3$ with X = I, Br and Cl), $CsPb(Br_xI_{1-x})_3$, $CsPb(Br_xCl_{1-x})_3$ PNCs,[169,176–178] and the combination of 2D perovskites and PNCs in hybrid nanocrystal materials (e.g., $PBABr_y(Cs_{0.7}FA_{0.3}PbBr_3)$)[179] were mostly used so far in PeLED applications, and achieved impressive EQEs of the devices in the past 5 years. The recent progress of PNC-based PeLED is shown in **Table 2** and **Figure 9**a. PNCs with various morphologies, namely 2D nanoplates, 1D nanowires, and 0D QDs can be utilized for PeLED applications.[171,172,175,176,180,181] Easy control of the halide content and quantum confinement effects allow the tunability of PNCs to enable PeLEDs that emit different colors (red, green, and blue).[169,170,176,181,182] The record EQE values for red, green, and blue-PeLEDs are 20.7%,[183] 20.3%,[184] and 9.5%,[179] respectively. For blue, green, and red perovskite QDs-based LEDs (PeQLEDs), the highest EQEs of 12.3%,[169] 22%,[169] and 21.3%[176] have been obtained with 0D cesium lead halide PNCs.

Tremendous work has been done to improve the stability and performance of PNC-based PeLED i) using short or zwitterionic sulfobetaine ligands in the PNCs synthesis,[185,186] 2) via metal ion doping to promote carrier injection ability of perovskites,[187,188] 3) upon addition of polymers,[189,190] 4) through surface passivation with metal halides/chlorides[178,180,191] or with a thin inorganic crystal layer at the grain boundary of PNCs to block ion migration, 5) via postsynthesis passivation (iminodibenzoic acid and didodecyldimethylammonium halides),[192,193] and finally 6) by optimizing the LED device structure, especially balancing the electron and the hole injection efficiency to reduce charge accumulation inside the device.

It is well known that the capping ligands (e.g., organic alkyl chain) severely influence the growth and optical properties of halide PNCs, thus, the theoretical simulation for the predicted effect of organic capping ligands on the PNCs is beneficial for the understanding of PL properties in close relation to their

ADVANCED
SCIENCE NEWS

www.advancedsciencenews.com

ADVANCED
PHOTONICS
RESEARCH
Open Access

www.adpr-journal.com

Table 2. Recent progress on red, green, and blue PNC-based PeLEDs.

Color	Emission layer	Turn on voltage [V]	EL wavelength [nm]	Maximum Luminance [cd m^{-2}]	Peak EQE [%]	Year of publishing	Ref.
Red	CsPbI$_3$ nanocrystal	2.2	698	206	5.7	2016/3	[181]
Red	CsPb(Br/I)$_3$ nanocrystals with PEI	1.9	648	2015	6.3	2016/10	[189]
Red	CsPb(Br/I)$_3$ nanocrystals with PEI	1.9	688	2216	7.25	2016/10	[189]
Red	CsPb(Br/I)$_3$ nanocrystals with PEI	1.9	648	2100	4.22	2016/10	[189]
Red	CsPbI$_3$ nanocrystals treat with IDA	4.5	688	748	5.02	2017/12	[192]
Red	CsPb(Br/I)$_3$ QDs with An-HI	2.6	645	500	14.1	2018/10	[176]
Red	CsPb(Br/I)$_3$ QDs with OAM-I	2.8	653	794	21.3	2018/10	[176]
Red	Sr^{2+}-doped CsPbI$_3$ nanocrystals		691	1152	13.5	2018/10	[178]
Red	Cu doped CsPbBrI$_2$ nanocrystals	4	630	2000	5.1	2019/5	[187]
Red	Sr^{2+-}substituted α-CsPbI$_3$QDs	9.2	678	1250	5.92	2019/1	[203]
Red	KBr with CsPbI$_{3-x}$Br$_x$ nanocrystals	3.6	637	2671	3.55	2020/1	[191]
Red	Zr-modified CsPbI$_3$ nanocrystals	3.9	686	14 725	13.7	2020/3	[202]
Green	CsPbBr$_3$ QDs	4.2	516	946	0.12	2015/10	[165]
Green	CsPbBr$_3$ nanocrystals		523	2335	0.19	2016/3	[181]
Green	CsPbBr$_3$-CsPb$_2$Br$_5$ nanocrystals	4.6	527	3853	2.21	2016/4	[237]
Green	CsPbBr$_3$ QDs	3.4	512	15 185	6.27	2016/11	[238]
Green	CH$_3$NH$_3$PbBr$_3$ nanocrystals	3.3	520		5.09	2017/6	[239]
Green	CsPbBr$_3$ QDs washed with AcOBu	2.7	512	1660	8.73	2017/5	[204]
Green	CsPbBr$_3$ QDs washed with BuOH	2.7	512	1490	6.25	2017/5	[204]
Green	PBA$_2$(CsPbBr$_3$)$_{n-1}$PbBr$_4$ nanoplates	8 V	514	14 000	10.4	2017/10	[175]
Green	OA/OLA-capped CsPbBr$_3$ nanocrystals	2.8	516	7085	6.5	2018/1	[185]
Green	CsPbBr$_3$ nanocrystals	3.5	516	1641	2.5	2018/2	[186]
Green	CsPbBr$_3$ QDs-DDAB	3.0	515		3.0	2016/8	[205]
Green	MAPbBr$_3$ nanocrystal	3.1	524	22 830	12.9	2018/4	[240]
Green	MAPbBr$_3$ nanocrystal	2.9	524	25 410	10.67	2018/4	[240]
Green	MAPbBr$_3$ nanocrystal	3.0	524	33 570	7.91	2018/4	[240]
Green	CsPbBr$_3$ QDs		515	55 800	11.6	2018/6	[207]
Green	FAPbBr$_3$ nanocrystals	4.7	526	13 970	16.3	2018/8	[172]
Green	CsPbBr$_3$ QDs passivated ZnBr$_2$		518	76 940	16.48	2018/10	[173]
Green	CsPbBr$_3$ QDs passivated MnBr$_2$		518	100 080	15.6	2018/10	[173]
Green	CsPbBr$_3$ QDs passivated GaBr$_3$		518	53 600	14.1	2018/10	[173]
Green	CsPbBr$_3$ QDs passivated InBr$_3$		518	76 200	16.2	2018/10	[173]
Green	CsPbBr$_3$ QDs		518	27 400	10.7	2018/10	[173]
Green	BA$_2$Cs$_{n-1}$Pb$_n$(Br/Y)$_{3n+1}$ nanoparticles	4.5	506	3810	10.1	2018/11	[241]
Green	DDAC/DDAB-treated CsPb(Br$_{1-x}$Cl$_x$)$_3$ nanocrystals		502	7600	4.96	2019/10	[193]
Green	DDAC/DDAB-treated CsPb(Br$_{1-x}$Cl$_x$)$_3$ nanocrystals		512	34 700	9.8	2019/10	[193]
Green	NaBr-based CsPbBr$_3$ nanoparticles	2.9	512	8353	17.4	2019/8	[188]
Green	CsPbBr$_3$ nanoparticles	2.9	516	7657	12.0	2019/8	[188]
Green	Bottom side TSPO1 passivated CsPbBr$_3$ QDs	6.8	516	11 000	10.2	2020/8	[177]
Green	Top side TSPO1 passivated CsPbBr$_3$ QDs	6.8	516	14 000	13.5	2020/8	[177]
Green	Bilateral interfacial passivated CsPbBr$_3$ QDs	6.8	516	21 000	18.7	2020/8	[177]
Green	Bipolar shell 7 nm CsPbBr$_3$		505	≈2000–3000	22	2020/7	[169]
Blue	CsPb(Br/Cl)$_3$ QDs	5.1	455	742	0.07	2015/10	[165]
Blue	CsPbBr$_x$Cl$_{3-x}$ nanocrystals			350	0.07	2017/4	[165]
Blue	CsPbBr$_3$ nanoplates		480	25	0.1	2018/3	[167]
Blue	Mn-doped CsPb(Br/Cl)$_3$ nanocrystals		466	245	2.2	2018/11	[180]

Table 2. Continued.

Color	Emission layer	Turn on voltage [V]	EL wavelength [nm]	Maximum Luminance [cd m^{-2}]	Peak EQE [%]	Year of publishing	Ref.
Blue	CsPbBr$_3$ QDs-DDAB	3.0	490	35	1.9	2016/8	[205]
Blue	PBABr$_y$(Cs$_{0.7}$FA$_{0.3}$PbBr$_3$) quantum-confined nanoparticlesuasi-2D phases	3.3	474		4	2019/8	[179]
Blue	PBABr$_y$(Cs$_{0.7}$FA$_{0.3}$PbBr$_3$) quantum-confined nanoparticles quasi-2D phases	3.3	476		4.8	2019/8	[179]
	PBABr$_y$(Cs$_{0.7}$FA$_{0.3}$PbBr$_3$) quantum-confined nanoparticles quasi-2D phases	3.4	478		6.3	2019/8	[179]
Blue	PBABr$_y$(Cs$_{0.7}$FA$_{0.3}$PbBr$_3$) quantum-confined nanoparticles quasi-2D phases	4.1	483	770	9.5	2019/8	[179]
Blue	BA$_2$Cs$_{n-1}$Pb$_n$(Br/Y)$_{3n+1}$ nanoparticles	5.0	465	962	2.4	2018/11	[241]
Blue	BA$_2$Cs$_{n-1}$Pb$_n$(Br/Y)$_{3n+1}$ nanoparticles	4.5	487	3340	6.2	2018/11	[241]
Blue	CsPb(Br/Cl)$_3$ nanocrystals	8.25	463	318	1.4	2019/5	[190]
Blue	DDAC/DDAB-treated CsPb(Br$_{1-x}$Cl$_x$)$_3$ nanocrystals		463	193	1.03	2019/10	[193]
Blue	DDAC/DDAB-treated CsPb(Br$_{1-x}$Cl$_x$)$_3$ nanocrystals		476	678	2.25	2019/10	[193]
Blue	DDAC/DDAB-treated CsPb(Br$_{1-x}$Cl$_x$)$_3$ nanocrystals		490	2063	3.5	2019/10	[193]
Blue	Ni^{2+}-doped CsPb(Br/Cl)$_3$ QDs	2.1	470	612	2.4	2020/2	[242]
Blue	DAT-treated CsPb(Br$_x$Cl$_{1-x}$)$_3$ QDs		470		6.3	2020/2	[206]
Blue	PBABr,C$_6$H$_5$(CH$_2$)$_4$NH$_3$Br	2.9	486	643.8	4.34	2020/4	[243]
Blue	PBABr,C$_6$H$_5$(CH$_2$)$_4$NH$_3$Br	2.7	493	1151	5.08	2020/4	[243]
Blue	Bipolar shell 4 nm CsPbBr$_3$	$\approx$2.6	479	$\approx$280–290	12.3	2020/7	[169]

performance in PeLED applications. Basically, the organic cations in perovskites negligibly contribute to the frontier molecular orbitals, so the focus of the DFT simulations can mainly focus on the inorganic lattice. On the other hand, the organic cations rather create the separation of the inorganic sheets and induce confinement from 3D to 2D.[194] Also, the alkyl chain length in the PNCs system effectively influences the bonding of the inorganic part. For instance, Kamminga et al. reported[195] that an increase in the ligand length reduces the angle of Pb—I—Pb to $\approx$153°. An excitonic band blue shift was also observed[196] with the decreasing structure dimensionality. Some DFT studies,[197,198] as well as a joint experimental and theoretical DFT,[199] on lead- and tin-based halides revealed the influence of the steric size of the organic cations on the bond angles of the inorganic lattice and on the bandgap as well. Accordingly, a reduced Pb—I—Pb bond angle is the result of the size increase in the organic molecules and the increase in the bandgap. This feature has been experimentally proved by observing a blue shift in the PL spectrum when the organic cation length was increased, so that the inorganic PbI$_2$ sheets were distorted.[195] For the aforementioned theoretical studies, the distorted bond angles, effective masses of the electrons and holes, and band structures were explored computationally through DFT + SOC analysis using the Quantum Espresso[200] software.

In general, long-chain organic ligands (such as oleic acid and oleylamine) shield the PNCs with an insulating layer, hence negatively impacting the performance and stability of PeLEDs.[185,192] In fact, the loss of surface ligands during washing and the presence of residual organics in the nanoparticles synthesized with a long-chain ligand can be very detrimental to the

charge-carrier transport of PNCs.[185] Both residual organics and surface trap sites formed by the loss of surface ligands act as nonradiative recombination centers, thus reducing the performance and PLQY of PeLEDs.[185] Hence, it is essential to synthesize PNCs with short-chain ligands (e.g., octylphosphonic acid [OPA]) to pursue high-performing devices.[185] For instance, PeLEDs fabricated with CsPbBr$_3$ PNCs synthesized with OPA ligands demonstrated an EQE of 6.5%, which is significantly higher than that of PNCs including long-chain ligands (EQE = 0.86%).[185]

More recently, Brown et al. reported an even higher EQE of 7.74% for a similar system.[201] Furthermore, Sr^{2+},[178] Cu^{2+},[192] Mn^{2+},[180] Zr$^+$,[202] NaBr,[188] and KBr[191] were added as additives/dopants into the perovskite precursor solution to enhance the stability and performance of PeLED by improving film morphology, charge transfer, emissive properties, and simultaneously passivate the nonradiative recombination surface trap sites.[178,180,188,191,192,202] For instance, the PLQY of CsPbBr$_3$ PNC-based films increased from 38% ± 5% to 68% ±5% upon the addition of 5% NaBr additive.[188] Consequently, the EQE was enhanced from 12% to 17.4% when 5% NaBr was added to CsPbBr$_3$ PNCs films,[188] resulting in the improved charge transport and defect passivation, along with the suppression of the defect-assisted nonradiative recombination.[188] The PLQYs of pristine CsPbI$_{3-x}$Br$_x$ and KBr-passivated CsPbI$_{3-x}$Br$_x$ PNC film were reported as 52% and 64%,[191] respectively. The inferior PLQY of pristine CsPbI$_{3-x}$Br$_x$ PNC film compared with the passivated one could be due to the surface defects that act as nonradiative recombination centers, similarly as discussed earlier.[191] The recombination scheme of excitons in pristine CsPbI$_{3-x}$Br$_x$ and KBr-passivated CsPbI$_{3-x}$Br$_x$ PNC films is
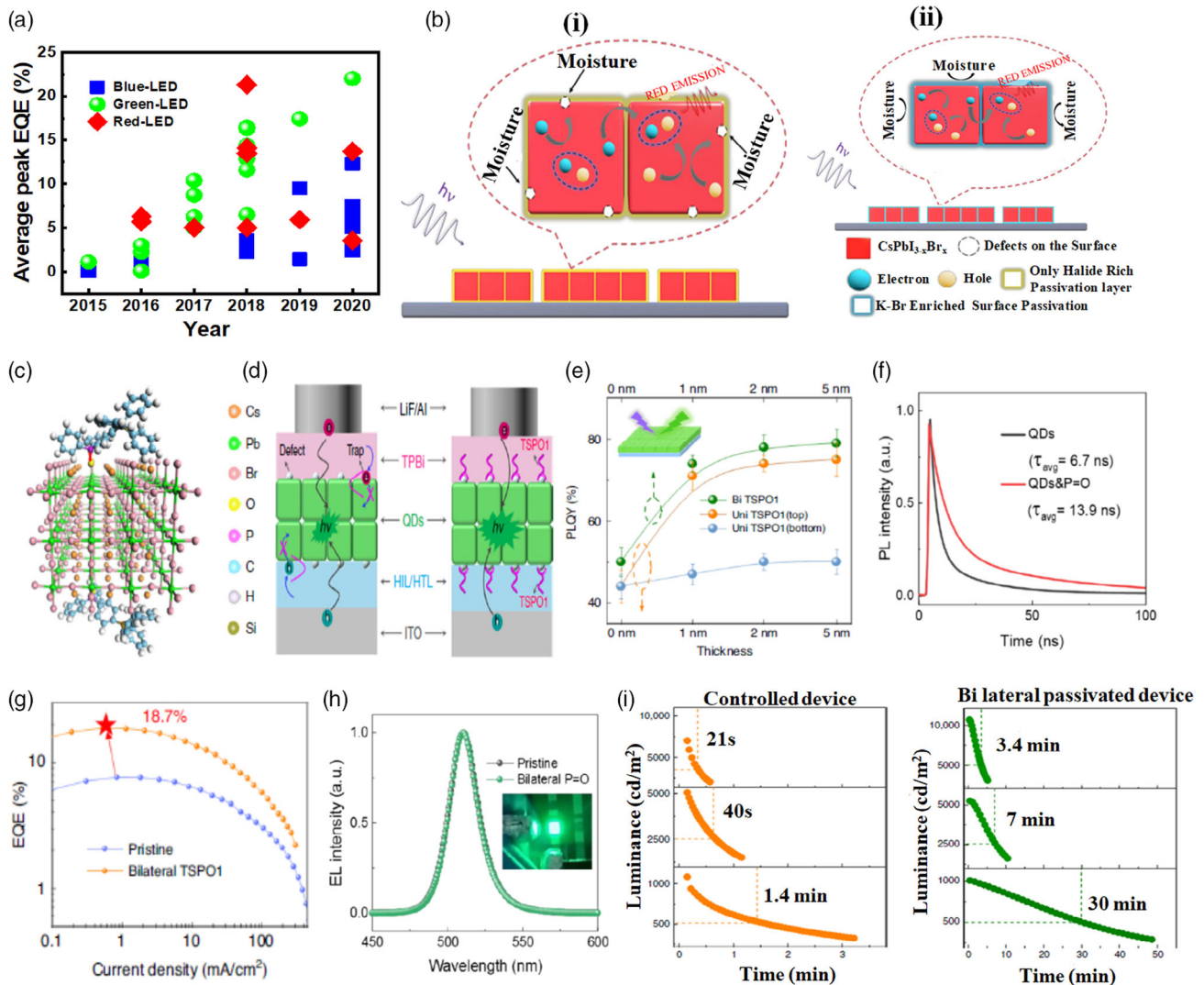
**ADVANCED
SCIENCE NEWS**

www.advancedsciencenews.com

**ADVANCED
PHOTONICS
RESEARCH**
Open Access

www.adpr-journal.com

Figure 9. a) Recent progress on blue, green, and red PNCs-based PeLED. b) Recombination of excitons in the CsPbI$_{3-x}$Br$_x$ PNC film: (i) pristine CsPbI$_{3-x}$Br$_x$ PNC film and (ii) KBr-passivated CsPbI$_{3-x}$Br$_x$ PNC film. Reproduced with permission.[191] Copyright 2020, American Chemical Society. c) Interaction between diphenylphosphine oxide-4-(triphenylsilyl)phenyl (TSPO1) ligand and perovskites QDs. The red double-headed arrow shows that the TSPO1 group interacts with the uncoordinated Pb atom. d) Structure of PQLED using passivated and not passivated QD films, and illustration on the role of TSPO1 in passivating defects on the surface of QD films. The defects may trap carriers (e.g., holes and electrons), decrease exciton recombination, and hence degrade the device performances. e) PLQY of QD films without and with TSPO1 on the bottom side, on the top side, and on both sides of QD film. f) PL decay curves of primal and TSPO1-passivated CsPbBr$_3$ QD films. g) EQE of the original device and bilateral-passivated device. h) Normalized EL spectra of pristine and bilateral-passivation QLEDs under an applied voltage of 3 V i) Operational lifetimes of pristine and bilateral-passivated device tested at different initial luminance, 1000, 5000, and 10 000 cd m^{-2}, respectively. Reproduced with permission.[177] Copyright 2020, Springer Nature.

shown in Figure 9b.[191] The defects were formed on the surface of the pristine CsPbI$_{3-x}$Br$_x$ PNC films when exposed to air, and these defects trap the excitons, thus leading to more nonradiative recombination (Figure 9b(i)). Nevertheless, the defect concentration in the case of KBr-containing PNCs film was minimized by the surface passivation of PNCs film with K$^+$ ions, leading to reduced nonradiative recombination (Figure 9b(ii)).[191] The highest EQE values were 3.55% and 1.89% for KBr-passivated CsPbI$_{3-x}$Br$_x$ PNCs and pure CsPbI$_{3-x}$Br$_x$ PNC-based PeLEDs,[191] respectively.

Highly efficient PeQLEDs based on 0D perovskite QD (PeQD) films can be realized as PeQDs display simultaneously bright luminescent features and effective electric transport properties.[166,169,173,176,177] The high luminescence of PeQD films is closely related to the quality of QD materials and their film formation process.[166,169,173,176,177] In fact, massive defects can form during the formation of the PeQD film, which significantly affects charge carrier injection, transportation, and recombination, and finally the degradation of the consequent PeQLED performance.[166,169,173,176,177] The development of PeQLEDs has

been going through two stages, i.e., an initial phase and an advanced phase. In the initial phase, lots of efforts were devoted to optimizing the quality of colloidal PeQDs so to improve the radiative recombination of PeQD films through surface ligand engineering, surface treatments (e.g., surface passivation), energy-level alignment, and new synthesis protocols to ensure halide-rich compositions.[180,203–207] The advanced phase of the development instead mainly focused on the passivation of defects located at the interface between the QD layer and charge selective layers, improving charge transport in QD films via, e.g., i) bipolar–shell resurface process, 2) substitution of the long organic ligands used during synthesis with short ligands, 3) anion exchange, and 4) interfacial engineering.[169,173,176,177,202] In the rest of this section, we will briefly summarize the key points from each of these strategies.

The surface treatment with long-chain organic ligands (e.g., DDAB) and bipolar shell resurfacing processes were implemented to address the bromide deficiency in purified PeQDs.[169] The bipolar shell-resurfaced PeQDs consist of an inner anion shell and an outer shell comprising cations and polar solvent molecules. The outer shell is electrostatically adsorbed to the negatively charged inner shell. This approach produces a short inter-QD distance enabling efficient charge transport in PeQD films as a result of the enhanced charge carrier mobility ($\geq 0.01 \, cm^2 \, V^{-1} \, s^{-1}$).[169] The bipolar shell-resurfaced 4 and 7 nm QDs exhibited near-unity PLQYs. The DDAB-treated 7 nm QDs showed a PLQY of 80%, whereas a notable increment in PLQY was not observed for DDAB-passivated 4 nm PeQDs.[169] The PLQY remained invariant over 6 months of shelf-storage confirming that bipolar shell-resurfaced PeQD solution indeed enabled excellent stability.[169] The operational lifetime of PeQLEDs constructed using bipolar shell PeQDs was 60 min at $1200 \, cd \, m^{-2}$ for the green LEDs and 20 min at $90 \, cd \, m^{-2}$, which was higher than the previously reported lifetime (<10 min).[169]

Song et al.[173] studied the impact of organic–inorganic hybrid ligand (OIHL) passivation on the chemical composition and the emissive properties of $CsPbBr_3$-based QD films. The halide-rich composition for OIHL-treated QDs was reported as a successful strategy to reduce the concentration of nonradiative recombination centers.[173] The PLQYs of OIHL-passivated PeQD films and pristine PeQD film-based devices have been reported as 79% and 58%, respectively. However, after annealing the films at 90 °C for 5 min, the PLQY of pristine QD film case decreased to 47% of the initial value with a reduction of 20%, whereas nearly 97% of the original value of PLQY was retained for OIHL-passivated QD films.[173] The PLQY decrease for thermal-annealed pristine PeQD films is possibly due to the high density of dangling bonds and uncoordinated surface atoms (e.g., Pb and halide vacancy) by solvent evaporation and the loss of surface ligands, which are accountable for the traps and nonradiative recombination.[173] The OIHL-passivated PeQLEDs demonstrated a higher current density ($875 \, mA \, cm^{-2}$) than that of pristine QDs ($761 \, mA \, cm^{-2}$) under the operating bias of 5.6 V. The average peak current efficiencies (average peak EQE values) from 40 devices were as high as $61.2 \, cd \, A^{-1}$ (15.1%), $59.6 \, cd \, A^{-1}$ (14.8%), $57.4 \, cd \, A^{-1}$ (13.8%), and $53.7 \, cd \, A^{-1}$ (14.6%) for LEDs based on $ZnBr^{2-}$, $MnBr^{2-}$, $InBr^{3-}$, and $GaBr^{3-}$-passivated PeQDs, respectively.[173] The PeQLED devices based on OIHL passivation have also shown a longer lifetime ($\approx 140 \, min$) than the case of the pristine PeQDs (40 min).[173]

The operational stability of PeQLEDs strongly depends on the environmental temperature, ion migration, thermal instability of the crystal phase, and interfacial instability.[166,173] Ion migration is generally associated with defect formation, interfacial charge and ion accumulation, degradation of interlayers, and corrosion of electrodes.[166,173] It is known that point defects, especially halide vacancies, serve as ion migration channels. Hence, the bromide-deficient pristine QDs favor ion migration under the bias, in turn leading to the PeQLEDs instability.[173]

Chiba et al. demonstrated anion-exchanged red-emitting PeQDs from pristine green-emitting $CsPbBr_3$ QDs using long alkyl chain-based oleylammonium iodide (OAM-I) and aryl-based aniline hydroiodide (An-HI) for the application in highly efficient LEDs.[176] After the anion-exchange, the red-emitting PeQDs in a toluene dispersion exhibited high PLQYs of 80% and 69% for OAM-I and An-HI, respectively. Indeed, the PLQY of the pristine $CsPbBr_3$ QDs was only 38%.[176] The higher PLQYs of the anion-exchanged red PeQDs versus the pristine ones was attributed to the hinding of anion defect formation. The EQE of the pristine $CsPbBr_3$ PeQLED was low (0.17%) due to the presence of anionic defects in the PeQDs.[176] On the other hand, the performances of the anion-exchanged red PeQLEDs were significantly enhanced. The averaged EQEs for the OAM-I and An-HI-passivated red PeQLEDs were 20.4% and 12.2%, respectively.[176] The OAM-I and An-HI-based PeQLED exhibited operational lifetimes of 5 min and 180 min, respectively.[176] The shorter lifetime of OAM-I-based PeQLED was attributed to the variation in chemical composition and surface ligands of the anion-exchanged PeQDs.[176] The bromide ion vacancy promotes ion migration in the device, and the presence of an electric field during device operation cause anion segregation in mixed-halide PeQDs, thus leading to the instability of the PeQLEDs.[166,173,176]

Xu et al. reported a bilateral interfacial passivation strategy for promoting the enhancement of the efficiency and stability of $CsPbBr_3$ PNCs-based PQLEDs.[177] The interaction between uncoordinated Pb present at the PeQD surface and P=O bond from the diphenylphosphine oxide-4-(triphenylsilyl)phenyl (TSPO1) ligand were highlighted as the critical factors that passivate the defects located at the interface of PeQD films and charge transport layer (Figure 9c,d).[177] In the PeQLEDs, the defects would capture electrons and holes, thus resulting in low device efficiency (Figure 9d). The as-synthesized cubic-shaped $CsPbBr_3$ QDs ink exhibited excellent PL properties with a PLQY of $85 \pm 3\%$.[177] Nevertheless, the light emission of the film exhibited a sharp decline ($43 \pm 4\%$) due to the formation of nonradiative recombination centers during the film-forming process.[177] The bilateral passivation through evaporation of organic ligands (TSPO1) on both top and bottom sides of perovskite QD films (Figure 9d,e) was anticipated to boost the PLQY and, thus, the exciton recombination efficiency.[177] Compared with both the bottom and top sides' passivation, bilateral passivation of QD films exhibited maximum PLQY of $79 \pm 3\%$ (Figure 9e), suggesting efficient electron−hole recombination in the passivated PeQD films.[177] The TSPO1-passivated films exhibited an average lifetime of approximately 13.9 ns that is longer than that of about 6.7 ns for primal QD films (Figure 9f), thus confirming that TSPO1 effectively reduces the nonradiative recombination centers on the QD films. The top and bottom sides of the

TSPO1-passivated device exhibited high EQE with peak values of 13.5% and 10.2% (Figure 9g), respectively. These values were higher than the EQE of the unpassivated devices (7.7%). Both side-passivated PeQLEDs exhibited an EQE as high as 18.7% (Figure 9g), whereas the EL spectra did not shift after the passivation (Figure 9h).[177] Both bilateral-passivated and unpassivated PeQLEDs exhibit an EL peak centered at 516 nm with an FWHM of 20 nm.[177] This indicates that the passivation layer would not affect the nanocrystal structure of the PeQDs. Furthermore, no spectrum shift was observed under the driving of different voltages.[177] Apart from the enhancement in exciton recombination (e.g., PL and EL efficiencies), bilateral passivation can also enhance the material and device stabilities.[177] The PL intensity of bilateral-passivated film exceeded 85% of the original value after 10 h, and the unilateral-passivated film retained 70% of the initial intensity, whereas the pure QD films lost 60% of the original intensity.[177] The pristine, unilateral-passivated, and bilateral-passivated PeQLED devices at a constant current density with an initial luminance of about 1000 cd m^{-2} exhibited operational lifetimes of 1.4, 14, and 30 min, respectively. For similar PeQLED devices at 100 cd m^{-2}, the operational lifetimes of pristine and bilateral passivation of the PeQLED device were predicted to be 47 min and 15.8 h, respectively.[177] The operational lifetimes of pristine (controlled) and bilateral-passivated devices under different initial luminance are shown in Figure 9i. This suggests that the higher the current density, the faster the device performance decay will be. All the results demonstrate that bilateral passivation is indeed an effective strategy to enhance the exciton recombination efficiency and thus increase the material and device stabilities.[177]

Fang et al. discussed the importance of controlling charge balance for fabricating high-performance green CsPbBr$_3$ QLED.[208] The simultaneous enhancement of EQE (21.63 %) and operational lifetime (180 h) was achieved by balancing the charge injection with the help of a bilayered electron transport structure (both electron blocking and hole transport layers).[208] Wang et al. studied the multifunction of the molecular interface (1,3,5-tris (bromomethyl) benzene (TBB))) control approach that reduces pinholes in the large-area perovskite layers, by controlling the film formation, and simultaneously passivates the defects in perovskites by incorporating Br species.[209] This approach prevents both shorts and nonradiative recombination, leading to improved charge injection or transport of PeQLEDs.[209] The green FAPbBr$_3$ nanocrystal PeLED, fabricated with a multifunctional molecular interface modifier, displayed a EQE of 20.1%.[209] The selection of interfacial layer materials is vital for obtaining a high-performance PeQLED.

Despite the notable accomplishments on blue, green, and red PeQLEDs, there is still much room to achieve stable and highly efficient red and blue devices with high luminance.[166,169,173,176,177,208,209] Though the maximum EQE of red PeQLED has been 21.1%, these devices' practical applications are limited by the color instability of PeQLED under operational conditions.[166,176] For instance, in mixed bromide–iodide perovskite emissive layers, Br and I ions tend to segregate into Br$^-$- and I$^-$-rich domains under the electric field, resulting in a shift of the EL spectra and change in emission colors during the device operation.[166,210] A similar phenomenon is observed in blue PeLEDs with mixed chloride–bromide perovskite emissive

layers.[181] Experimental and theoretical calculations suggest that phase segregation is mediated by ionic defects, especially by vacancies.[211] Serious attention is required to in-depth investigate defect passivation to cope up with the ion migration pathways.

7.2. Lead-Free-based PeLEDs

The high toxicity of lead ions in traditional perovskite-based LEDs may limit their commercial viability. The high-water solubility of lead halide perovskites enables the release of lead into groundwater resources, impacting environmental pollution and human health.[166] It is essential to search for alternative compounds that are environmentally friendly while maintaining the device's performance of Pb-based perovskites. Wide ranges of promising lead-free materials have exhibited PLQYs comparable with lead halide perovskites.[159,212–222] The lead-free counterparts include copper halides (Cs$_3$Cu$_2$I$_5$, Rb$_2$CuX$_3$, K$_2$CuX$_3$, X = Br, Cl), CsSnX$_3$ (X = I, Br), Cs$_3$Sb$_2$Br$_9$, FA$_3$Bi$_2$Br$_9$, (OCTAm)$_2$SnBr$_4$, PEA$_2$SnI$_4$, CH$_3$NH$_3$Sn(Br$_{1-x}$I$_x$)$_3$, vacancy-ordered halide double perovskites (Bi-Cs$_2$SnI$_6$, Cs$_2$Sn$_{1-x}$Te$_x$Cl$_6$), and halide double perovskites (Cs$_2$Ag$_x$Na$_{1-x}$InCl$_6$, Cs$_2$AgInCl$_6$, Cs$_2$AgBiBr$_6$), (C$_4$N$_2$H$_{14}$Br)$_4$SnBr$_6$, which display near unity PLQYs.[159,212–227] The Cs$_3$Cu$_2$I$_5$-based LED has shown a low EQE of 1.1% and exhibited a high operational time (109 h).[159] The maximum EQE of 5% was demonstrated for PEA$_2$SnI$_4$-based LEDs made with valeric acid (VA), and they have also shown an operating time of 15 h.[225] The position of EL spectra does not change even after 9 h operation.[225] The enhanced device stability is attributed to the strong interactions between VA and the perovskite film, suppressing ion migration during device operation and preventing tin oxidation.[225] The tin-based multiple quantum well PeLED displays an EQE of 3%, and these devices show an operational time of 2 h under a constant current density of 10 mA cm^{-2}.[228] Recently, substantial progress has been made on lead-free PeLEDs, as shown in **Table 3**. However, the design rules need to be further developed to screen promising materials from the plethora of possible lead-free perovskite emitters for LED applications.[159,212–222] The large tolerance on exciton binding energies, bandgaps, and charge-carrier mobility of the materials have a critical role in obtaining high device performance.[159,212–222] A combination of experimental and theoretical investigations on exciton binding energies, bandgaps, and charge-carrier mobilities may help to search for the suitable lead-free materials for high-performance LEDs.[159,212–222]

8. Conclusions

Halide PNCs are the rising star in optoelectronics, especially when considering the light-emitting applications, due to their outstanding luminescence. In this Review, we have summarized recent findings on the light emission of PNCs. We especially focused on the correlation between PL and phase transition, the dual-color emission, the tunability of the PL toward NIR, and the thermal quenching effect. The utilization of PNCs in illuminating devices, i.e., LEDs, has been also discussed as their core application, due to the typically high PLQY of halide PNCs. Although a huge number of interesting research works have been reported in the PNCs field within the last 5 years, there

Table 3. Recent progress lead-free-based PeLEDs.

Color	Emission layer	Turn on voltage [V]	EL wavelength [nm]	Maximum luminance [cd m^{-2}]	Peak EQE [%]	Year of publishing	Ref.
Infared	$CH_3NH_3Sn(Br_{1-x}I_x)_3$	2.2	945	58	0.72	2016/6	[244]
Red	$CH_3NH_3Sn(Br_{1-x}I_x)_3$	2.2	667	209	0.007	2016/6	[244]
Infared	$CsSnI_3$ thin film	≈2.0	950	364.3	3.8	2016/7	[245]
Red	PEA_2SnI_4 films	3.6	618		0.15	2017/6	[227]
Red	$CsSnBr_3$ thin film		673		0.34	2018/3	[227]
UV	$Cs_2Ag_{0.6}Na_{0.4}InCl_6$:Bi			5000		2018/11	[215]
Red	$(OAm)_2SnBr_4$	2.2	621	350	0.1	2018/12	[246]
Infared	$(PEAI)_2(CsI)_3(SnI_2)_3$ films	2.0			0.25	2019/1	[228]
Infared	$(PEAI)_2(CsI)_5(SnI_2)_6$ films	2.0			1.52	2019/1	[228]
Infared	$(PEAI)_{3.5}(CsI)_5(SnI_2)_{4.5}$ films	2.0	920		3.01	2019/1	[228]
Blue	$Cs_3Sb_2Br_9$ QDs	5.0	408	29.6	0.21	2019/11	[227]
Red	TEA_2SnI_4 thin film	2.23	638	322	0.62	2020/1	[247]
Red	PEA_2SnI_4 thin film	2.30	629	58	0.16	2020/1	[247]
Yellow	$CsCu_2I_3$ thin film	5.0	555/571	47.5	0.17	2020/6	[248]
Blue	$Cs_3Cu_2I_5$ thin film		436/	140	0.27	2020/5	[248]
Blue	$Cs_3Cu_2I_5$ thin film	4.5	437/460	262.6	1.12	2020/6	[159]
Red	PEA_2SnI_4 thin film	5.8	633	70	0.3	2020/4	[226]
Red	$(PEA)_2SnI_4$ film with VA		632	170	5	2020/10	[225]
Red	$(PEA)_2SnI_4$ film		632	38	0.13	2020/10	[225]

is still large room for further improving their luminescence performance with strong potential for a broad range of applications in optoelectronics.

In this section, we provide our critical view on relevant investigation directions for further development of luminescent PNCs: 1) Deep understanding of the PL properties with fundamental mechanism studies, particularly for lead-free-based PNCs. Lead-free PNCs, whereas on the one hand allow addressing the toxicity concern of lead-based PNCs, on the other hand display poor luminescent properties, i.e., low PLQY and low defect-tolerance, compared with the highly luminescent lead-based ones. As quite many lead-free PNCs (e.g., Bi-based and Sb-based) display indirect transition features (one key reasons for the low PLQY), it is urgent to clarify their underlying luminescent mechanisms such as radiative recombination pathways, intraband states, and direct–indirect transitions. The outcomes of these studies will provide crucial hints for electronic structure engineering to enhance the PLQY. 2) Passivating the PNC surface via doping engineering for the enhancement of the luminescence. It is undoubtedly important to probe the effects of various metal cations (e.g., transition metals and rare-earth metals) on surface passivation, and on the traps or vacancies filling. Though the doping of PNCs has already recently been the focus of many reports, we believe that this strategy could still be successfully adopted to improve the optoelectronic properties of the host PNCs, whereas at the same time, overcoming some of the critical challenges of PNCs, e.g., stability. For instance, Sn^{2+}-based PNCs normally exhibit extremely low PLQY (e.g., <1%) due to their intrinsic high density of vacancies, thus, doping of Sn-PNCs with some divalent metal cations, such as Mn^{2+}, could be an effective way to improve their PLQY while potentially

stabilizing the Sn^{2+} against its easy oxidization in air. 3) Advanced modeling studies for the accurate prediction of emission-related properties. Currently, DFT is typically used to study the band structure, density of states, and charge carrier (electron and hole) effective mass of PNCs. Expanding the scope of theoretical calculations to pursue more accurate prediction of, e.g., the quality assessment of as-formed halide PNCs (number of defects and impurities per unit PNC), the role of metal cations in nonradiative quenching, and the origin of the emissive centers, may enable further exciting advancement in the understanding of the emission properties of PNCs. In this respect, more attention should be also paid to fine-tune the selection of the most appropriate computational method to specifically study the nanocrystal systems. Recently, the classical force-field method has been adopted for the PNCs modeling to overcome the limitations of DFT related to the high number of atoms of the systems under consideration,[229] the presence of ligands (the size of ligands is commonly not considered), and the interactions with the solvent that are typically neglected. Moreover, the classical force-field calculations require considerably less time than the corresponding DFT ones. 4) Broadening the emission-related applications toward commercialization. Most of the current studies on PNCs' applications focus on the direct applications of light-emitting materials such as LEDs, photodetectors, and lasing. Nevertheless, there are several other possible exploitations of the emission properties of halide PNCs, e.g., temperature sensor (thermochromism of 0D Cs_4PbBr_6),[230] upconversion luminescence ($CsPb(Br/I)_3$ NCs),[231] stress sensor (pressure-induced emission in Cs_4PbBr_6 NCs),[232] and superfluorescence from PNC superlattices (for multiphoton quantum light sources).[233] Another intriguing consequence of both quantum confinement

and high PLQYs of PNCs is their application in scintillators. Lead halide PNCs exhibit strong radioluminescence (X-ray excited emission) intensities with tunable emission energies.[234] The scintillating sensitivity of PNCs is much higher than that of commercial scintillators, such as $PbWO_4$ and $YAlO_3$:Ce. The investigation of PNCs, and particularly Pb-free PNCs, with their bright radioluminescence intensities, can be a promising area of research to be further expanded. For instance, the radio-luminescence intensity of Rb_2CuBr_3 (91 000 photons/MeV) is 4 times higher than that of $CsPbBr_3$ PNCs (21 000 photons/MeV) and also outperforms several well-known scintillators.[235]

5) Improving the emission stability of PNCs at elevated temperatures. The emission TQ of PNCs has been reduced by encapsulating them in an inorganic matrix (PNC-hybrids). As a result, the PNC-hybrids have been proposed as potential color emitters in phosphor-converted white LED (pc-WLED) applications. However, their emission TQ remains higher than that of conventional phosphor materials. One possibility to reduce the emission TQ of PNCs-based pc-WLED is to encapsulate them in structurally robust oxide- and nitride-based inorganic hosts. For example, lanthanide-doped inorganic phosphors showed almost no emission intensity loss even at high temperatures (e.g., $200\,°C$)[192] upon oxide- and nitride-hosts encapsulation. This strategy could be promisingly further explored and extended also to PNC-based phosphors in the future.

Acknowledgements

Conflict of Interest

The authors declare no conflict of interest.

Keywords

[1] L. C. Schmidt, A. Pertegás, S. González-Carrero, O. Malinkiewicz, S. Agouram, G. Mínguez Espallargas, H. J. Bolink, R. E. Galian, J. Pérez-Prieto, *J. Am. Chem. Soc.* **2014**, *136*, 850.

[2] L. Protesescu, S. Yakunin, M. I. Bodnarchuk, F. Krieg, R. Caputo, C. H. Hendon, R. X. Yang, A. Walsh, M. V. Kovalenko, *Nano Lett.* **2015**, *15*, 3692.

[3] G. Nedelcu, L. Protesescu, S. Yakunin, M. I. Bodnarchuk, M. J. Grotevent, M. V. Kovalenko, *Nano Lett.* **2015**, *15*, 5635.

[4] S. Adjokatse, H. H. Fang, M. A. Loi, *Mater. Today* **2017**, *20*, 413.

[5] J. Chen, K. Žídek, P. Chábera, D. Liu, P. Cheng, L. Nuuttila, M. J. Al-Marri, H. Lehtivuori, M. E. Messing, K. Han, K. Zheng, T. Pullerits, *J. Phys. Chem. Lett.* **2017**, *8*, 2316.

[6] Q. A. Akkerman, V. D'Innocenzo, S. Accornero, A. Scarpellini, A. Petrozza, M. Prato, L. Manna, *J. Am. Chem. Soc.* **2015**, *137*, 10276.

[7] G. R. Yettapu, D. Talukdar, S. Sarkar, A. Swarnkar, A. Nag, P. Ghosh, P. Mandal, *Nano Lett.* **2016**, *16*, 4838.

[8] M. Liu, H. Zhang, D. Gedamu, P. Fourmont, H. Rekola, A. Hiltunen, S. G. Cloutier, R. Nechache, A. Priimagi, P. Vivo, *Small* **2019**, *15*, 1900801.

[9] J. Song, J. Li, X. Li, L. Xu, Y. Dong, H. Zeng, *Adv. Mater.* **2015**, *27*, 7162.

[10] N. Mondal, A. De, A. Samanta, *ACS Energy Lett.* **2019**, *4*, 32.

[11] A. Swarnkar, A. R. Marshall, E. M. Sanehira, B. D. Chernomordik, D. T. Moore, J. A. Christians, T. Chakrabarti, J. M. Luther, *Science* **2016**, *354*, 92.

[12] M. Liu, H. Pasanen, H. Ali-Löytty, A. Hiltunen, K. Lahtonen, S. Qudsia, J.-H. Smått, M. Valden, N. Tkachenko, P. Vivo, *Angew. Chem., Int. Ed.* **2020**, *59*, 22117.

[13] P. Ramasamy, D.-H. Lim, B. Kim, S.-H. Lee, M.-S. Lee, J.-S. Lee, *Chem. Commun.* **2016**, *52*, 2067.

[14] I. M. Asuo, P. Fourmont, I. Ka, D. Gedamu, S. Bouzidi, A. Pignolet, R. Nechache, S. G. Cloutier, *Small* **2018**, *15*, 1804150.

[15] Y. Wang, X. Li, J. Song, L. Xiao, H. Zeng, H. Sun, *Adv. Mater.* **2015**, *27*, 7101.

[16] T. Umebayashi, K. Asai, T. Umebayashi, K. Asai, T. Kondo, T. Kondo, A. Nakao, *Phys. Rev. B – Condens. Matter Mater. Phys.* **2003**, *67*, 155405.

[17] C. M. Wang, Y. M. Su, T. A. Shih, G. Y. Chen, Y. Z. Chen, C. W. Lu, I. S. Yu, Z. P. Yang, H. C. Su, *J. Mater. Chem. C* **2018**, *6*, 12808.

[18] J. Shamsi, A. S. Urban, M. Imran, L. De Trizio, L. Manna, *Chem. Rev.* **2019**, *119*, 3296.

[19] C. Qin, T. Matsushima, W. J. Potscavage, A. S. D. Sandanayaka, M. R. Leyden, F. Bencheikh, K. Goushi, F. Mathevet, B. Heinrich, G. Yumoto, Y. Kanemitsu, C. Adachi, *Nat. Photonics* **2020**, *14*, 70.

[20] R. L. Z. Hoye, A. Fakharuddin, D. N. Congreve, J. Wang, L. Schmidt-Mende, *APL Mater.* **2020**, *8*, 70401.

[21] Z. Cheng, J. Lin, *CrystEngComm* **2010**, *12*, 2646.

[22] X. Li, F. Cao, D. Yu, J. Chen, Z. Sun, Y. Shen, Y. Zhu, L. Wang, Y. Wei, Y. Wu, H. Zeng, *Small* **2017**, *13*, 1603996.

[23] D. Chen, X. Chen, *J. Mater. Chem. C* **2019**, *7*, 1413.

[24] M. Liu, A. Matuhina, H. Zhang, P. Vivo, *Materials* **2019**, *12*, 3733.

[25] D. Cortecchia, J. Yin, A. Petrozza, C. Soci, *J. Mater. Chem. C* **2019**, *7*, 4956.

[26] Z. Song, J. Zhao, Q. Liu, *Inorg. Chem. Front.* **2019**, *6*, 2969.

[27] M. D. Smith, B. A. Connor, H. I. Karunadasa, *Chem. Rev.* **2019**, *119*, 3104.

[28] J. Shamsi, A. S. Urban, M. Imran, L. De Trizio, L. Manna, *Chem. Rev.* **2019**, *119*, 3296.

[29] W. Li, Z. Wang, F. Deschler, S. Gao, R. H. Friend, A. K. Cheetham, *Nat. Rev. Mater.* **2017**, *2*, 16099.

[30] M. V. Kovalenko, L. Protesescu, M. I. Bodnarchuk, *Science* **2017**, *358*, 745.

[31] L. Protesescu, S. Yakunin, S. Kumar, J. Bär, F. Bertolotti, N. Masciocchi, A. Guagliardi, M. Grotevent, I. Shorubalko, M. I. Bodnarchuk, C.-J. Shih, M. V. Kovalenko, *ACS Nano* **2017**, *11*, 3119.

[32] F. Palazon, G. Almeida, Q. A. Akkerman, L. De Trizio, Z. Dang, M. Prato, L. Manna, *Chem. Mater.* **2017**, *29*, 4167.

[33] T. Udayabhaskararao, L. Houben, H. Cohen, M. Menahem, I. Pinkas, L. Avram, T. Wolf, A. Teitelboim, M. Leskes, O. Yaffe, D. Oron, M. Kazes, *Chem. Mater.* **2018**, *30*, 84.

[34] X. Chen, D. Chen, J. Li, G. Fang, H. Sheng, J. Zhong, *Dalt. Trans.* **2018**, *47*, 5670.

[35] Z. Liu, Y. Bekenstein, X. Ye, S. C. Nguyen, J. Swabeck, D. Zhang, S.-T. Lee, P. Yang, W. Ma, A. P. Alivisatos, *J. Am. Chem. Soc.* **2017**, *139*, 5309.

[36] G. Li, H. Wang, Z. Zhu, Y. Chang, T. Zhang, Z. Song, Y. Jiang, *Chem. Commun.* **2016**, *52*, 11296.

[37] S. K. Balakrishnan, P. V. Kamat, *Chem. Mater.* **2018**, *30*, 74.

[38] W. Shen, L. Ruan, Z. Shen, Z. Deng, *Chem. Commun.* **2018**, *54*, 2804.

[39] G. Xiao, Y. Cao, G. Qi, L. Wang, C. Liu, Z. Ma, X. Yang, Y. Sui, W. Zheng, B. Zou, *J. Am. Chem. Soc.* **2017**, *139*, 10087.

[40] F. Palazon, C. Urso, L. De Trizio, Q. Akkerman, S. Marras, F. Locardi, I. Nelli, M. Ferretti, M. Prato, L. Manna, *ACS Energy Lett.* **2017**, *2*, 2445.

[41] L. Wu, H. Hu, Y. Xu, S. Jiang, M. Chen, Q. Zhong, D. Yang, Q. Liu, Y. Zhao, B. Sun, Q. Zhang, Y. Yin, *Nano Lett.* **2017**, *17*, 5799.

[42] P. E. Blöchl, *Phys. Rev. B* **1994**, *50*, 17953.

[43] D. M. Jang, K. Park, D. H. Kim, J. Park, F. Shojaei, H. S. Kang, J.-P. Ahn, J. W. Lee, J. K. Song, *Nano Lett.* **2015**, *15*, 5191.

[44] W. Geng, L. Zhang, Y.-N. Zhang, W.-M. Lau, L.-M. Liu, *J. Phys. Chem. C* **2014**, *118*, 19565.

[45] K. Schötz, A. M. Askar, A. Köhler, K. Shankar, F. Panzer, *Adv. Opt. Mater.* **2020**, *8*, 2000455.

[46] D. Priante, I. Dursun, M. S. Alias, D. Shi, V. A. Melnikov, T. K. Ng, O. F. Mohammed, O. M. Bakr, B. S. Ooi, *Appl. Phys. Lett.* **2015**, *106*, 081902.

[47] X. Fang, K. Zhang, Y. Li, L. Yao, Y. Zhang, Y. Wang, W. Zhai, L. Tao, H. Du, G. Ran, *Appl. Phys. Lett.* **2016**, *108*, 071109.

[48] W. Kong, Z. Ye, Z. Qi, B. Zhang, M. Wang, A. Rahimi-Iman, H. Wu, *Phys. Chem. Chem. Phys.* **2015**, *17*, 16405.

[49] B. Wu, H. T. Nguyen, Z. Ku, G. Han, D. Giovanni, N. Mathews, H. J. Fan, T. C. Sum, *Adv. Energy Mater.* **2016**, *6*, 1600551.

[50] B. Murali, S. Dey, A. L. Abdelhady, W. Peng, E. Alarousu, A. R. Kirmani, N. Cho, S. P. Sarmah, M. R. Parida, M. I. Saidaminov, A. A. Zhumekenov, J. Sun, M. S. Alias, E. Yengel, B. S. Ooi, A. Amassian, O. M. Bakr, O. F. Mohammed, *ACS Energy Lett.* **2016**, *1*, 1119.

[51] Y. Fang, H. Wei, Q. Dong, J. Huang, *Nat. Commun.* **2017**, *8*, 14417.

[52] Y. H. Qiu, F. Nan, Q. Wang, X. D. Liu, S. J. Ding, Z. H. Hao, L. Zhou, Q. Q. Wang, *J. Phys. Chem. C* **2017**, *121*, 6916.

[53] K. Schötz, A. M. Askar, W. Peng, D. Seeberger, T. P. Gujar, M. Thelakkat, A. Köhler, S. Huettner, O. M. Bakr, K. Shankar, F. Panzer, *J. Mater. Chem. C* **2020**, *8*, 2289.

[54] T. Wang, B. Daiber, J. M. Frost, S. A. Mann, E. C. Garnett, A. Walsh, B. Ehrler, *Energy Environ. Sci.* **2017**, *10*, 509.

[55] J. A. Steele, P. Puech, B. Monserrat, B. Wu, R. X. Yang, T. Kirchartz, H. Yuan, G. Fleury, D. Giovanni, E. Fron, M. Keshavarz, E. Debroye, G. Zhou, T. C. Sum, A. Walsh, J. Hofkens, M. B. J. Roeffaers, *ACS Energy Lett.* **2019**, *4*, 2205.

[56] R. Chulia-Jordan, E. Mas-Marzá, A. Segura, J. Bisquert, J. P. Martínez-Pastor, *J. Phys. Chem. C* **2018**, *122*, 22717.

[57] B. Wu, H. Yuan, Q. Xu, J. A. Steele, D. Giovanni, P. Puech, J. Fu, Y. F. Ng, N. F. Jamaludin, A. Solanki, S. Mhaisalkar, N. Mathews, M. B. J. Roeffaers, M. Grätzel, J. Hofkens, T. C. Sum, *Nat. Commun.* **2019**, *10*, 484.

[58] Y. S. Park, S. Guo, N. S. Makarov, V. I. Klimov, *ACS Nano* **2015**, *9*, 10386.

[59] B. W. Park, B. Philippe, X. Zhang, H. Rensmo, G. Boschloo, E. M. J. Johansson, *Adv. Mater.* **2015**, *27*, 6806.

[60] J.-C. Hebig, I. Kühn, J. Flohre, T. Kirchartz, *ACS Energy Lett.* **2016**, *1*, 309.

[61] A. H. Slavney, T. Hu, A. M. Lindenberg, H. I. Karunadasa, *J. Am. Chem. Soc.* **2016**, *138*, 2138.

[62] E. T. McClure, M. R. Ball, W. Windl, P. M. Woodward, *Chem. Mater.* **2016**, *28*, 1348.

[63] Y. Zhang, J. Yin, M. R. Parida, G. H. Ahmed, J. Pan, O. M. Bakr, J.-L. Brédas, O. F. Mohammed, *J. Phys. Chem. Lett.* **2017**, *8*, 3173.

[64] B. Yang, X. Mao, F. Hong, W. Meng, Y. Tang, X. Xia, S. Yang, W. Deng, K. Han, *J. Am. Chem. Soc.* **2018**, *140*, 17001.

[65] A. Dey, A. F. Richter, T. Debnath, H. Huang, L. Polavarapu, J. Feldmann, *ACS Nano* **2020**, *14*, 5855.

[66] N. Pradhan, S. Das Adhikari, A. Nag, D. D. Sarma, *Angew. Chem., Int. Ed.* **2017**, *56*, 7038.

[67] F. Meinardi, Q. A. Akkerman, F. Bruni, S. Park, M. Mauri, Z. Dang, L. Manna, S. Brovelli, *ACS Energy Lett.* **2017**, *2*, 2368.

[68] S. Zou, Y. Liu, J. Li, C. Liu, R. Feng, F. Jiang, Y. Li, J. Song, H. Zeng, M. Hong, X. Chen, *J. Am. Chem. Soc.* **2017**, *139*, 11443.

[69] K. Bai, R. Zeng, B. Ke, S. Cao, X. Xue, R. Tan, B. Zou, *J. Alloys Compd.* **2019**, *806*, 858.

[70] Z. Chen, H. Chen, C. Zhang, L. Chen, Z. Qin, H. Sang, X. Wang, M. Xiao, *Appl. Phys. Lett.* **2019**, *114*, 041902.

[71] J. Ghosh, M. Hossain, P. K. Giri, *J. Colloid Interface Sci.* **2020**, *564*, 357.

[72] W. Wang, J. Li, G. Duan, H. Zhou, Y. Lu, T. Yan, B. Cao, Z. Liu, *J. Alloys Compd.* **2020**, *821*, 153568.

[73] K. Xu, A. Meijerink, *Chem. Mater.* **2018**, *30*, 5346.

[74] W. Chen, X. Tang, Z. Zang, Y. Shi, Z. Yang, J. Du, *Nanotechnology* **2019**, *30*, 075704.

[75] T. Qiao, D. Parobek, Y. Dong, E. Ha, D. H. Son, *Nanoscale* **2019**, *11*, 5247.

[76] W. Liu, Q. Lin, H. Li, K. Wu, I. Robel, J. M. Pietryga, V. I. Klimov, *J. Am. Chem. Soc.* **2016**, *138*, 14954.

[77] Q. A. Akkerman, D. Meggiolaro, Z. Dang, F. De Angelis, L. Manna, *ACS Energy Lett.* **2017**, *2*, 2183.

[78] M. He, Y. Cheng, L. Shen, H. Zhang, C. Shen, W. Xiang, X. Liang, *J. Am. Ceram. Soc.* **2019**, *102*, 1090.

[79] Q. Ba, A. Jana, L. Wang, K. S. Kim, *Adv. Funct. Mater.* **2019**, *29*, 1904768.

[80] K. Xing, X. Yuan, Y. Wang, J. Li, Y. Wang, Y. Fan, L. Yuan, K. Li, Z. Wu, H. Li, J. Zhao, *J. Phys. Chem. Lett.* **2019**, *10*, 4177.

[81] W. van der Stam, J. J. Geuchies, T. Altantzis, K. H. W. van den Bos, J. D. Meeldijk, S. Van Aert, S. Bals, D. Vanmaekelbergh, C. de Mello Donega, *J. Am. Chem. Soc.* **2017**, *139*, 4087.

[82] R. Begum, M. R. Parida, A. L. Abdelhady, B. Murali, N. M. Alyami, G. H. Ahmed, M. N. Hedhili, O. M. Bakr, O. F. Mohammed, *J. Am. Chem. Soc.* **2017**, *139*, 731.

[83] R. Martín-Rodríguez, A. Geitenbeek, A. Meijerink, *J. Am. Chem. Soc.* **2013**, *135*, 13668.

[84] D. J. Norris, A. L. Efros, S. C. Erwin, *Science (80-.)* **2008**, *319*, 1776.

[85] D. Zhou, D. Liu, G. Pan, X. Chen, D. Li, W. Xu, X. Bai, H. Song, *Adv. Mater.* **2017**, *29*, 1704149.

[86] Q. Hu, Z. Li, Z. Tan, H. Song, C. Ge, G. Niu, J. Han, J. Tang, *Adv. Opt. Mater.* **2018**, *6*, 1700864.

[87] J. S. Yao, J. Ge, B. N. Han, K. H. Wang, H. Bin Yao, H. L. Yu, J. H. Li, B. S. Zhu, J. Z. Song, C. Chen, Q. Zhang, H. B. Zeng, Y. Luo, S. H. Yu, *J. Am. Chem. Soc.* **2018**, *140*, 3626.

[88] N. Chen, T. Cai, W. Li, K. Hills-Kimball, H. Yang, M. Que, Y. Nagaoka, Z. Liu, D. Yang, A. Dong, C. Y. Xu, R. Zia, O. Chen, *ACS Appl. Mater. Interfaces* **2019**, *11*, 16855.

[89] S. Paul, E. Bladt, A. F. Richter, M. Döblinger, Y. Tong, H. Huang, A. Dey, S. Bals, T. Debnath, L. Polavarapu, J. Feldmann, *Angew. Chem., Int. Ed.* **2020**, *59*, 6794.

[90] E. Hemmer, N. Venkatachalam, H. Hyodo, A. Hattori, Y. Ebina, H. Kishimoto, K. Soga, *Nanoscale* **2013**, *5*, 11339.

[91] J. O. Escobedo, O. Rusin, S. Lim, R. M. Strongin, *Curr. Opin. Chem. Biol.* **2010**, *14*, 64.

[92] I. V. Martynenko, A. P. Litvin, F. Purcell-Milton, A. V. Baranov, A. V. Fedorov, Y. K. Gun'ko, *J. Mater. Chem. B* **2017**, *5*, 6701.

[93] E. H. Sargent, *Adv. Mater.* **2008**, *20*, 3958.

[94] A. L. Rogach, A. Eychmüller, S. G. Hickey, S. V. Kershaw, *Small* **2007**, *3*, 536.

[95] C. Gendrin, Y. Roggo, C. Collet, *J. Pharm. Biomed. Anal.* **2008**, *48*, 533.

[96] A. Shrestha, M. Batmunkh, A. Tricoli, S. Z. Qiao, S. Dai, *Angew. Chem., Int. Ed.* **2019**, *58*, 5202.

[97] J. C. G. Bünzli, S. V. Eliseeva, *J. Rare Earths* **2010**, *28*, 824.

[98] P. Vashishtha, S. Bishnoi, C.-H. A. Li, M. Jagadeeswararao, T. J. N. Hooper, N. Lohia, S. B. Shivarudraiah, M. S. Ansari, S. N. Sharma, J. E. Halpert, *ACS Appl. Electron. Mater.* **2020**, *2*, 3470.

[99] F. Zhang, H. Zhong, C. Chen, X. Wu, X. Hu, H. Huang, J. Han, B. Zou, Y. Dong, *ACS Nano* **2015**, *9*, 4533.

[100] D. M. Jang, D. H. Kim, K. Park, J. Park, J. W. Lee, J. K. Song, *J. Mater. Chem. C* **2016**, *4*, 10625.

[101] I. Levchuk, A. Osvet, X. Tang, M. Brandl, J. D. Perea, F. Hoegl, G. J. Matt, R. Hock, M. Batentschuk, C. J. Brabec, *Nano Lett.* **2017**, *17*, 2765.

[102] M. Li, R. Begum, J. Fu, Q. Xu, T. M. Koh, S. A. Veldhuis, M. Grätzel, N. Mathews, S. Mhaisalkar, T. C. Sum, *Nat. Commun.* **2018**, *9*, 4197.

[103] L. Protesescu, S. Yakunin, S. Kumar, J. Bär, F. Bertolotti, N. Masciocchi, A. Guagliardi, M. Grotevent, I. Shorubalko, M. I. Bodnarchuk, C. J. Shih, M. V. Kovalenko, *ACS Nano* **2017**, *11*, 3119.

[104] H. Huang, M. I. Bodnarchuk, S. V. Kershaw, M. V. Kovalenko, A. L. Rogach, *ACS Energy Lett.* **2017**, *2*, 2071.

[105] F. Xu, T. Zhang, G. Li, Y. Zhao, *J. Mater. Chem. A* **2017**, *5*, 11450.

[106] J. A. Steele, M. Lai, Y. Zhang, Z. Lin, J. Hofkens, M. B. J. Roeffaers, P. Yang, *Accounts Mater. Res.* **2020**, *1*, 3.

[107] R. J. Sutton, G. E. Eperon, L. Miranda, E. S. Parrott, B. A. Kamino, J. B. Patel, M. T. Hörantner, M. B. Johnston, A. A. Haghighirad, D. T. Moore, H. J. Snaith, *Adv. Energy Mater.* **2016**, *6*, 1502458.

[108] D. Chen, X. Chen, Z. Wan, G. Fang, *ACS Appl. Mater. Interfaces* **2017**, *9*, 20671.

[109] A. Hazarika, Q. Zhao, E. A. Gaulding, J. A. Christians, B. Dou, A. R. Marshall, T. Moot, J. J. Berry, J. C. Johnson, J. M. Luther, *ACS Nano* **2018**, *12*, 10327.

[110] R. Begum, X. Y. Chin, M. Li, B. Damodaran, T. C. Sum, S. Mhaisalkar, N. Mathews, *Chem. Commun.* **2019**, *55*, 5451.

[111] I. Lignos, V. Morad, Y. Shynkarenko, C. Bernasconi, R. M. Maceiczyk, L. Protesescu, F. Bertolotti, S. Kumar, S. T. Ochsenbein, N. Masciocchi, A. Guagliardi, C. J. Shih, M. I. Bodnarchuk, A. J. Demello, M. V. Kovalenko, *ACS Nano* **2018**, *12*, 5504.

[112] W. Xiang, W. Tress, *Adv. Mater.* **2019**, *31*, 1902851.

[113] B. Du, Y. Xia, Q. Wei, G. Xing, Y. Chen, W. Huang, *ChemNanoMat* **2019**, *5*, 266.

[114] F. Liu, C. Ding, Y. Zhang, T. S. Ripolles, T. Kamisaka, T. Toyoda, S. Hayase, T. Minemoto, K. Yoshino, S. Dai, M. Yanagida, H. Noguchi, Q. Shen, *J. Am. Chem. Soc.* **2017**, *139*, 16708.

[115] P. Xu, S. Chen, H. J. Xiang, X. G. Gong, S. H. Wei, *Chem. Mater.* **2014**, *26*, 6068.

[116] T. C. Jellicoe, J. M. Richter, H. F. J. Glass, M. Tabachnyk, R. Brady, S. E. Dutton, A. Rao, R. H. Friend, D. Credgington, N. C. Greenham, M. L. Böhm, *J. Am. Chem. Soc.* **2016**, *138*, 2941.

[117] F. Liu, J. Jiang, Y. Zhang, C. Ding, T. Toyoda, S. Hayase, R. Wang, S. Tao, Q. Shen, *Angew. Chem., Int. Ed.* **2020**, *59*, 8421.

[118] A. B. Wong, Y. Bekenstein, J. Kang, C. S. Kley, D. Kim, N. A. Gibson, D. Zhang, Y. Yu, S. R. Leone, L. W. Wang, A. P. Alivisatos, P. Yang, *Nano Lett.* **2018**, *18*, 2060.

[119] Y. Zhou, Y. Zhao, *Energy Environ. Sci.* **2019**, *12*, 1495.

[120] Q. Fan, G. V. Biesold-McGee, J. Ma, Q. Xu, S. Pan, J. Peng, Z. Lin, *Angew. Chem., Int. Ed.* **2020**, *59*, 1030.

[121] C. H. Lu, G. V. Biesold-McGee, Y. Liu, Z. Kang, Z. Lin, *Chem. Soc. Rev.* **2020**, *49*, 4953.

[122] W. J. Mir, T. Sheikh, H. Arfin, Z. Xia, A. Nag, *NPG Asia Mater.* **2020**, *12*, 9.

[123] G. Pan, X. Bai, D. Yang, X. Chen, P. Jing, S. Qu, L. Zhang, D. Zhou, J. Zhu, W. Xu, B. Dong, H. Song, *Nano Lett.* **2017**, *17*, 8005.

[124] W. J. Mir, Y. Mahor, A. Lohar, M. Jagadeeswararao, S. Das, S. Mahamuni, A. Nag, *Chem. Mater.* **2018**, *30*, 8170.

[125] T. J. Milstein, K. T. Kluherz, D. M. Kroupa, C. S. Erickson, J. J. De Yoreo, D. R. Gamelin, *Nano Lett.* **2019**, *19*, 1931.

[126] Q. Y. Zhang, X. Y. Huang, *Prog. Mater. Sci.* **2010**, *55*, 353.

[127] J. Zhou, Y. Teng, S. Zhou, J. Qiu, *Int. J. Appl. Glas. Sci.* **2012**, *3*, 299.

[128] X. Zhang, Y. Zhang, X. Zhang, W. Yin, Y. Wang, H. Wang, M. Lu, Z. Li, Z. Gu, W. W. Yu, *J. Mater. Chem. C* **2018**, *6*, 10101.

[129] X. Luo, T. Ding, X. Liu, Y. Liu, K. Wu, *Nano Lett.* **2019**, *19*, 338.

[130] J. Shi, F. Li, J. Yuan, X. Ling, S. Zhou, Y. Qian, W. Ma, *J. Mater. Chem. A* **2019**, *7*, 20936.

[131] Y. Mahor, W. J. Mir, A. Nag, *J. Phys. Chem. C* **2019**, *123*, 15787.

[132] W. Lee, S. Hong, S. Kim, *J. Phys. Chem. C* **2019**, *123*, 2665.

[133] H. Arfin, J. Kaur, T. Sheikh, S. Chakraborty, A. Nag, *Angew. Chem., Int. Ed.* **2020**, *59*, 11307.

[134] D. Chen, G. Fang, X. Chen, *ACS Appl. Mater. Interfaces* **2017**, *9*, 40477.

[135] K. Xu, C. C. Lin, X. Xie, A. Meijerink, *Chem. Mater.* **2017**, *29*, 4265.

[136] X. Yuan, S. Ji, M. C. De Siena, L. Fei, Z. Zhao, Y. Wang, H. Li, J. Zhao, D. R. Gamelin, *Chem. Mater.* **2017**, *29*, 8003.

[137] O. Meza, E. G. Villabona-Leal, L. A. Diaz-Torres, H. Desirena, J. L. Rodríguez-López, E. Pérez, *J. Phys. Chem. A* **2014**, *118*, 1390.

[138] W. Q. Peng, S. C. Qu, G. W. Cong, Z. G. Wang, *J. Cryst. Growth* **2005**, *279*, 454.

[139] S. Bera, N. Pradhan, *ACS Energy Lett.* **2020**, *5*, 2858.

[140] X. Zhang, X. Wu, X. Liu, G. Chen, Y. Wang, J. Bao, X. Xu, X. Liu, Q. Zhang, K. Yu, W. Wei, J. Liu, J. Xu, H. Jiang, P. Wang, X. Wang, *J. Am. Chem. Soc.* **2020**, *142*, 4464.

[141] M. Amachraa, Z. Wang, C. Chen, S. Hariyani, H. Tang, J. Brgoch, S. P. Ong, *Chem. Mater.* **2020**, *32*, 6256.

[142] D. N. Dirin, B. M. Benin, S. Yakunin, F. Krumeich, G. Raino, R. Frison, M. V. Kovalenko, *ACS Nano* **2019**, *13*, 11642.

[143] Y. Zhuo, A. Mansouri Tehrani, A. O. Oliynyk, A. C. Duke, J. Brgoch, *Nat. Commun.* **2018**, *9*, 4377.

[144] B. T. Diroll, G. Nedelcu, M. V. Kovalenko, R. D. Schaller, *Adv. Funct. Mater.* **2017**, *27*, 1606750.

[145] X. Yuan, X. Hou, J. Li, C. Qu, W. Zhang, J. Zhao, H. Li, *Phys. Chem. Chem. Phys.* **2017**, *19*, 8934.

[146] H. C. Woo, J. W. Choi, J. Shin, S.-H. Chin, M. H. Ann, C.-L. Lee, *J. Phys. Chem. Lett.* **2018**, *9*, 4066.

[147] H. Fang, L. Protesescu, D. M. Balazs, S. Adjokatse, M. V. Kovalenko, M. A. Loi, *Small* **2017**, *13*, 1700673.

[148] S. Kahmann, O. Nazarenko, S. Shao, O. Hordiichuk, M. Kepenekian, J. Even, M. V. Kovalenko, G. R. Blake, M. A. Loi, *ACS Energy Lett.* **2020**, *5*, 2512.

[149] H. Barkaoui, H. Abid, S. Zelewski, J. Urban, M. Baranowski, A. Mlayah, S. Triki, P. Plochocka, Y. Abid, *Adv. Opt. Mater.* **2019**, *7*, 1900763.

[150] H.-C. Wang, S.-Y. Lin, A.-C. Tang, B. P. Singh, H.-C. Tong, C.-Y. Chen, Y.-C. Lee, T.-L. Tsai, R.-S. Liu, *Angew. Chem., Int. Ed.* **2016**, *55*, 7924.

[151] M. Palei, M. Imran, G. Biffi, L. Manna, F. Di Stasio, R. Krahne, *ACS Appl. Nano Mater.* **2020**, *3*, 8167.

[152] D. Chen, Z. Wan, X. Chen, Y. Yuan, J. Zhong, *J. Mater. Chem. C* **2016**, *4*, 10646.

[153] G. K. Grandhi, N. S. M. Viswanath, H. B. Cho, S. M. Kim, W. B. Im, *Nanoscale* **2019**, *11*, 21137.

**ADVANCED
SCIENCE NEWS**

www.advancedsciencenews.com

**ADVANCED
PHOTONICS
RESEARCH**
Open Access

www.adpr-journal.com

[154] G. K. Grandhi, N. S. M. Viswanath, J. H. In, H. B. Cho, W. B. Im, *J. Phys. Chem. Lett.* **2020**, *11*, 3699.

[155] P. Vashishtha, G. V. Nutan, B. E. Griffith, Y. Fang, D. Giovanni, M. Jagadeeswararao, T. C. Sum, N. Mathews, S. G. Mhaisalkar, J. V. Hanna, *Chem. Mater.* **2019**, *31*, 9003.

[156] S. Yakunin, B. M. Benin, Y. Shynkarenko, O. Nazarenko, M. I. Bodnarchuk, D. N. Dirin, C. Hofer, S. Cattaneo, M. V. Kovalenko, *Nat. Mater.* **2019**, *18*, 846.

[157] T. Jun, K. Sim, S. Iimura, M. Sasase, H. Kamioka, J. Kim, H. Hosono, *Adv. Mater.* **2018**, *30*, 1804547.

[158] V. Morad, S. Yakunin, M. V. Kovalenko, *ACS Mater. Lett.* **2020**, *2*, 845.

[159] L. Wang, Z. Shi, Z. Ma, D. Yang, F. Zhang, X. Ji, M. Wang, X. Chen, G. Na, S. Chen, D. Wu, Y. Zhang, X. Li, L. Zhang, C. Shan, *Nano Lett.* **2020**, *20*, 3568.

[160] R. Lin, Q. Zhu, Q. Guo, Y. Zhu, W. Zheng, F. Huang, *J. Phys. Chem. C* **2020**, *124*, 20469.

[161] G. K. Grandhi, N. S. M. Viswanath, H. Bin Cho, J. H. Han, S. M. Kim, S. Choi, W. Bin Im, *J. Phys. Chem. Lett.* **2020**, *11*, 7723.

[162] X. Zhao, J. D. A. Ng, R. H. Friend, Z. Tan, *ACS Photonics* **2018**, *5*, 3866.

[163] X. Zhao, Z. Tan, *Nat. Photonics* **2020**, *14*, 215.

[164] S. Do, A. Sadhanala, C. G. Park, S. Rhee, S. H. Im, *ACS Nano* **2017**, *11*, 6586.

[165] J. Song, J. Li, X. Li, L. Xu, Y. Dong, H. Zeng, *Adv. Mater.* **2015**, *27*, 7162.

[166] X. Liu, W. Xu, S. Bai, Y. Jin, J. Wang, R. H. Friend, F. Gao, *Nat. Mater.* **2020**, https://doi.org/10.1038/s41563-020-0784-7.

[167] D. Yang, Y. Zou, P. Li, Q. Liu, L. Wu, H. Hu, Y. Xu, B. Sun, Q. Zhang, S. Lee, *Nano Energy* **2018**, *47*, 235.

[168] M. Lu, Y. Zhang, S. Wang, J. Guo, W. W. Yu, A. L. Rogach, *Adv. Funct. Mater.* **2019**, *29*, 1902008.

[169] Y. Dong, Y. Wang, F. Yuan, A. Johnston, Y. Liu, D. Ma, M. Choi, B. Chen, M. Chekini, S. Baek, L. K. Sagar, J. Fan, Y. Hou, M. Wu, S. Lee, B. Sun, S. Hoogland, R. Quintero-bermudez, H. Ebe, P. Todorovic, F. Dinic, P. Li, H. T. Kung, M. I. Saidaminov, E. Kumacheva, E. Spiecker, L. Liao, O. Voznyy, Z. Lu, E. H. Sargent, *Nat. Nanotechnol.* **2020**, *15*, 668.

[170] Y. H. Kim, H. Cho, T. W. Lee, *Proc. Natl. Acad. Sci. U. S. A.* **2016**, *113*, 11694.

[171] F. Yan, J. Xing, G. Xing, L. Quan, S. T. Tan, J. Zhao, R. Su, H. V. Demir, *Nano Lett.* **2018**, *18*, 3157.

[172] D. Han, M. Imran, M. Zhang, S. Chang, X. G. Wu, X. Zhang, J. Tang, M. Wang, S. Ali, X. Li, G. Yu, J. Han, L. Wang, B. Zou, H. Zhong, *ACS Nano* **2018**, *12*, 8808.

[173] J. Song, T. Fang, J. Li, L. Xu, F. Zhang, B. Han, *Adv. Mater.* **2018**, *30*, 1805409.

[174] Z. Ren, L. Li, J. Yu, R. Ma, X. Xiao, R. Chen, K. Wang, X. W. Sun, W. Yin, W. C. H. Choy, *ACS Energy Lett.* **2020**, *5*, 2569.

[175] J. Si, Y. Liu, Z. He, H. Du, K. Du, D. Chen, J. Li, M. Xu, H. Tian, H. He, D. Di, C. Lin, Y. Cheng, J. Wang, Y. Jin, *ACS Nano* **2017**, *11*, 11100.

[176] T. Chiba, Y. Hayashi, H. Ebe, K. Hoshi, J. Sato, S. Sato, Y. J. Pu, S. Ohisa, J. Kido, *Nat. Photonics* **2018**, *12*, 681.

[177] L. Xu, J. Li, B. Cai, H. Zeng, *Nat. Commun.* **2020**, *11*, 3902.

[178] M. Lu, X. Zhang, Y. Zhang, J. Guo, X. Shen, W. W. Yu, A. L. Rogach, *Adv. Mater.* **2018**, *30*, 1804691.

[179] Y. Liu, J. Cui, K. Du, H. Tian, Z. He, Q. Zhou, Z. Yang, Y. Deng, D. Chen, X. Zuo, Y. Ren, L. Wang, H. Zhu, B. Zhao, D. Di, J. Wang, R. H. Friend, Y. Jin, *Nat. Photonics* **2019**, *13*, 760.

[180] S. Hou, K. Mahesh, Q. Quan, S. Hou, M. K. Gangishetty, Q. Quan, D. N. Congreve, *Joule* **2018**, *2*, 2421.

[181] G. Li, F. Wisnivesky, R. Rivarola, N. J. L. K. Davis, S. Bai, T. C. Jellicoe, F. De Peña, S. Hou, C. Ducati, F. Gao, R. H. Friend, N. C. Greenham, Z. Tan, *Adv. Mater.* **2016**, *28*, 3528.

[182] L. N. Quan, F. P. García de Arquer, R. P. Sabatini, E. H. Sargent, *Adv. Mater.* **2018**, *30*, 1801996.

[183] Y. Cao, N. Wang, H. Tian, J. Guo, Y. Wei, H. Chen, Y. Miao, W. Zou, K. Pan, Y. He, H. Cao, Y. Ke, M. Xu, Y. Wang, M. Yang, K. Du, Z. Fu, D. Kong, D. Dai, Y. Jin, G. Li, H. Li, Q. Peng, J. Wang, W. Huang, *Nature* **2018**, *562*, 249.

[184] K. Lin, J. Xing, L. N. Quan, F. P. G. de Arquer, X. Gong, J. Lu, L. Xie, W. Zhao, D. Zhang, C. Yan, W. Li, X. Liu, Y. Lu, J. Kirman, E. H. Sargent, Q. Xiong, Z. Wei, *Nature* **2018**, *562*, 245.

[185] Y. Tan, Y. Zou, L. Wu, Q. Huang, D. Yang, M. Chen, M. Ban, C. Wu, T. Wu, S. Bai, T. Song, Q. Zhang, B. Sun, *ACS Appl. Mater. Interfaces* **2018**, *10*, 3784.

[186] F. Krieg, S. T. Ochsenbein, S. Yakunin, S. Ten Brinck, P. Aellen, A. Süess, B. Clerc, D. Guggisberg, O. Nazarenko, Y. Shynkarenko, S. Kumar, C. J. Shih, I. Infante, M. V. Kovalenko, *ACS Energy Lett.* **2018**, *3*, 641.

[187] H. Chen, L. Fan, R. Zhang, W. Liu, Q. Zhang, R. Guo, S. Zhuang, L. Wang, *Adv. Opt. Mater.* **2019**, *7*, 1900747.

[188] J. Zhang, L. Zhang, P. Cai, X. Xue, M. Wang, J. Zhang, G. Tu, *Nano Energy* **2019**, *62*, 434.

[189] X. Zhang, C. Sun, Y. Zhang, H. Wu, C. Ji, Y. Chuai, P. Wang, *J. Phys. Chem. Lett.* **2016**, *7*, 4602.

[190] S. T. Ochsenbein, F. Krieg, Y. Shynkarenko, G. Rainò, M. V. Kovalenko, *ACS Appl. Mater. Interfaces* **2019**, *11*, 21655.

[191] J. Yang, Y. Song, J. Yao, K. Wang, J. Wang, B. Zhu, M. Yao, S. U. Rahman, Y. Lan, F. Fan, H. Yao, *J. Am. Chem. Soc.* **2020**, *142*, 2956.

[192] J. Pan, Y. Shang, J. Yin, M. De Bastiani, W. Peng, I. Dursun, L. Sinatra, A. M. El-zohry, M. N. Hedhili, A. Emwas, O. F. Mohammed, Z. Ning, O. M. Bakr, *J. Am. Chem. Soc.* **2018**, *140*, 562.

[193] Y. Shynkarenko, M. I. Bodnarchuk, C. Bernasconi, Y. Berezovska, V. Verteletskyi, S. T. Ochsenbein, M. V. Kovalenko, *ACS Energy Lett.* **2019**, *4*, 2703.

[194] G. C. Papavassiliou, I. B. Koutselas, A. Terzis, M. H. Whangbo, *Solid State Commun.* **1994**, *91*, 695.

[195] M. E. Kamminga, H.-H. Fang, M. R. Filip, F. Giustino, J. Baas, G. R. Blake, M. A. Loi, T. T. M. Palstra, *Chem. Mater.* **2016**, *28*, 4554.

[196] G. C. Papavassiliou, *Mol. Cryst. Liq. Cryst. Sci. Technol. Sect. A* **1996**, *286*, 231.

[197] J. L. Knutson, J. D. Martin, D. B. Mitzi, *Inorg. Chem.* **2005**, *44*, 4699.

[198] M. R. Filip, G. E. Eperon, H. J. Snaith, F. Giustino, *Nat. Commun.* **2014**, *5*, 5757.

[199] L. Mao, H. Tsai, W. Nie, L. Ma, J. Im, C. C. Stoumpos, C. D. Malliakas, F. Hao, M. R. Wasielewski, A. D. Mohite, M. G. Kanatzidis, *Chem. Mater.* **2016**, *28*, 7781.

[200] P. Giannozzi, S. Baroni, N. Bonini, M. Calandra, R. Car, C. Cavazzoni, D. Ceresoli, G. L. Chiarotti, M. Cococcioni, I. Dabo, A. Dal Corso, S. de Gironcoli, S. Fabris, G. Fratesi, R. Gebauer, U. Gerstmann, C. Gougoussis, A. Kokalj, M. Lazzeri, L. Martin-Samos, N. Marzari, F. Mauri, R. Mazzarello, S. Paolini, A. Pasquarello, L. Paulatto, C. Sbraccia, S. Scandolo, G. Sclauzero, A. P. Seitsonen, A. Smogunov, P. Umari, R. M. Wentzcovitch, *J. Phys. Condens. Matter* **2009**, *21*, 395502.

[201] A. A. M. Brown, T. J. N. Hooper, S. A. Veldhuis, X. Y. Chin, A. Bruno, P. Vashishtha, J. N. Tey, L. Jiang, B. Damodaran, S. H. Pu, S. G. Mhaisalkar, N. Mathews, *Nanoscale* **2019**, *11*, 12370.

[202] M. Lu, J. Guo, S. Sun, P. Lu, J. Wu, Y. Wang, S. V. Kershaw, W. W. Yu, A. L. Rogach, Y. Zhang, *Nano Lett.* **2020**, *20*, 2829.

[203] J. Yao, J. Ge, K. Wang, G. Zhang, B. Zhu, C. Chen, Q. Zhang, Y. Luo, S. Yu, H. Yao, *J. Am. Chem. Soc.* **2019**, *141*, 2069.

[204] T. Chiba, K. Hoshi, Y.-J. Pu, Y. Takeda, Y. Hayashi, S. Ohisa, S. Kawata, J. Kido, *ACS Appl. Mater. Interfaces* **2017**, *9*, 18054.

**ADVANCED
SCIENCE NEWS**

www.advancedsciencenews.com

**ADVANCED
PHOTONICS
RESEARCH**

www.adpr-journal.com

[205] J. Pan, L. N. Quan, Y. Zhao, W. Peng, B. Murali, S. P. Sarmah, M. Yuan, L. Sinatra, N. M. Alyami, J. Liu, E. Yassitepe, Z. Yang, O. Voznyy, R. Comin, M. N. Hedhili, O. F. Mohammed, Z. H. Lu, D. H. Kim, E. H. Sargent, *Adv. Mater.* **2016**, *39*, 8718.

[206] M. Wei, C. Zhou, K. Song, B. Zhang, Y. Lin, M. N. Hedhili, N. Wehbe, Y. Han, H. Sun, Z. Lu, T. D. Anthopoulos, O. F. Mohammed, E. H. Sargent, L. Liao, O. M. Bakr, *ACS Energy Lett.* **2020**, *5*, 793.

[207] J. Song, J. Li, L. Xu, J. Li, F. Zhang, B. Han, *Adv. Mater.* **2018**, *30*, 1800764.

[208] T. Fang, T. Wang, X. Li, Y. Dong, S. Bai, J. Song, *Sci. Bull.* **2020**, *3*, 1.

[209] H. Wang, X. Gong, D. Zhao, Y. B. Zhao, S. Wang, J. Zhang, L. Kong, B. Wei, R. Quintero-Bermudez, O. Voznyy, Y. Shang, Z. Ning, Y. Yan, E. H. Sargent, X. Yang, *Joule* **2020**, *4*, 1977.

[210] P. Vashishtha, J. E. Halpert, *Chem. Mater.* **2017**, *29*, 5965.

[211] Y. Yuan, J. Huang, *Acc. Chem. Res.* **2016**, *49*, 286.

[212] J. Luo, X. Wang, S. Li, J. Liu, Y. Guo, G. Niu, L. Yao, Y. Fu, L. Gao, Q. Dong, C. Zhao, M. Leng, F. Ma, W. Liang, L. Wang, S. Jin, J. Han, L. Zhang, J. Etheridge, J. Wang, Y. Yan, E. H. Sargent, J. Tang, *Nature* **2018**, *563*, 541.

[213] G. Xiong, L. Yuan, Y. Jin, H. Wu, Z. Li, B. Qu, G. Ju, L. Chen, S. Yang, Y. Hu, *Adv. Opt. Mater.* **2020**, *8*, 2000779.

[214] H. Chen, J. M. Pina, F. Yuan, F. Yuan, A. Johnston, D. Ma, B. Chen, Z. Li, A. Dumont, X. Li, Y. Liu, S. Hoogland, Z. Zajacz, Z. Lu, E. H. Sargent, *J. Phys. Chem. Lett.* **2020**, *11*, 4326.

[215] Y. Wu, X. Li, H. Zeng, *ACS Energy Lett.* **2019**, *4*, 673.

[216] R. Roccanova, A. Yangui, H. Nhalil, H. Shi, M.-H. Du, B. Saparov, *ACS Appl. Electron. Mater.* **2019**, *1*, 269.

[217] R. Zhang, X. Mao, D. Zheng, Y. Yang, S. Yang, K. Han, *Laser Photonics Rev.* **2020**, *14*, 2000027.

[218] M. Leng, Y. Yang, K. Zeng, Z. Chen, Z. Tan, S. Li, J. Li, B. Xu, D. Li, M. P. Hautzinger, Y. Fu, T. Zhai, L. Xu, G. Niu, S. Jin, J. Tang, *Adv. Funct. Mater.* **2018**, *28*, 1704446.

[219] T. D. Creason, T. M. McWhorter, Z. Bell, M.-H. Du, B. Saparov, *Chem. Mater.* **2020**, *32*, 6197.

[220] C. Zhou, H. Lin, Y. Tian, Z. Yuan, R. Clark, B. Chen, L. J. Van De Burgt, J. C. Wang, Y. Zhou, K. Hanson, Q. J. Meisner, J. Neu, T. Besara, T. Siegrist, E. Lambers, P. Djurovich, B. Ma, *Chem. Sci.* **2018**, *9*, 586.

[221] Z. Tan, Y. Chu, J. Chen, J. Li, G. Ji, G. Niu, L. Gao, Z. Xiao, J. Tang, *Adv. Mater.* **2020**, *32*, 1.

[222] Y. Li, P. Vashishtha, Z. Zhou, Z. Li, S. B. Shivarudraiah, C. Ma, J. Liu, K. S. Wong, H. Su, J. E. Halpert, *Chem. Mater.* **2020**, *32*, 5515.

[223] Y. Shen, J. Yin, B. Cai, Z. Wang, Y. Dong, X. Xu, H. Zeng, *Nanoscale Horizons* **2020**, *5*, 580.

[224] T. Xuan, R. J. Xie, *Chem. Eng. J.* **2020**, *393*, 124757.

[225] F. Yuan, X. Zheng, A. Johnston, Y. Wang, C. Zhou, Y. Dong, B. Chen, H. Chen, J. Z. Fan, G. Sharma, P. Li, Y. Gao, O. Voznyy, H. Kung, Z. Lu, O. M. Bakr, E. H. Sargent, *Sci. Adv.* **2020**, *6*, 42.

[226] H. Liang, F. Yuan, A. Johnston, C. Gao, H. Choubisa, Y. Gao, Y. K. Wang, L. K. Sagar, B. Sun, P. Li, G. Bappi, B. Chen, J. Li, Y. Wang, Y. Dong, D. Ma, Y. Gao, Y. Liu, M. Yuan, M. I. Saidaminov, S. Hoogland, Z. H. Lu, E. H. Sargent, *Adv. Sci.* **2020**, *7*, 1903213.

[227] Z. Ma, L. Wang, X. Ji, X. Chen, Z. Shi, *J. Phys. Chem. Lett.* **2020**, *11*, 5517.

[228] Y. Wang, R. Zou, J. Chang, Z. Fu, Y. Cao, L. Zhang, Y. Wei, D. Kong, W. Zou, K. Wen, N. Fan, N. Wang, W. Huang, J. Wang, *J. Phys. Chem. Lett.* **2019**, *10*, 453.

[229] B. Zhang, M. Wang, M. Ghini, A. E. M. Melcherts, J. Zito, L. Goldoni, I. Infante, M. Guizzardi, F. Scotognella, I. Kriegel, L. De Trizio, L. Manna, *ACS Mater. Lett.* **2020**, *27*, 1442.

[230] J. W. Choi, N. Cho, H. C. Woo, B. M. Oh, J. Almutlaq, O. M. Bakr, S. H. Kim, C. L. Lee, J. H. Kim, *Nanoscale* **2019**, *11*, 5754.

[231] Z. Duan, Y. Wang, G. Li, S. Wang, N. Yi, S. Liu, S. Xiao, Q. Song, *Laser Photonics Rev.* **2018**, *12*, 1700234.

[232] Z. Ma, Z. Liu, S. Lu, L. Wang, X. Feng, D. Yang, K. Wang, G. Xiao, L. Zhang, S. A. T. Redfern, B. Zou, *Nat. Commun.* **2018**, *9*, 1.

[233] G. Rainò, M. A. Becker, M. I. Bodnarchuk, R. F. Mahrt, M. V. Kovalenko, T. Stöferle, *Nature* **2018**, *563*, 671.

[234] Q. Chen, J. Wu, X. Ou, B. Huang, J. Almutlaq, A. A. Zhumekenov, X. Guan, S. Han, L. Liang, Z. Yi, J. Li, X. Xie, Y. Wang, Y. Li, D. Fan, D. B. L. Teh, A. H. All, O. F. Mohammed, O. M. Bakr, T. Wu, M. Bettinelli, H. Yang, W. Huang, X. Liu, *Nature* **2018**, *561*, 88.

[235] B. Yang, L. Yin, G. Niu, J. Yuan, K. Xue, Z. Tan, X. Miao, M. Niu, X. Du, H. Song, E. Lifshitz, J. Tang, *Adv. Mater.* **2019**, *31*, 1904711.

[236] S. Das Adhikari, S. K. Dutta, A. Dutta, A. K. Guria, N. Pradhan, *Angew. Chem., Int. Ed.* **2017**, *129*, 8872.

[237] X. Zhang, B. Xu, J. Zhang, Y. Gao, Y. Zheng, K. Wang, *Adv. Funct. Mater.* **2016**, *26*, 4595.

[238] J. Li, L. Xu, T. Wang, J. Song, J. Chen, J. Xue, Y. Dong, B. Cai, Q. Shan, B. Han, H. Zeng, *Adv. Mater.* **2017**, *29*, 1603885.

[239] Y. H. Kim, C. Wolf, Y. T. Kim, H. Cho, W. Kwon, S. Do, A. Sadhanala, C. G. Park, S. W. Rhee, S. H. Im, R. H. Friend, T. W. Lee, *ACS Nano* **2017**, *11*, 6586.

[240] F. Yan, J. Xing, G. Xing, L. Quan, S. T. Tan, J. Zhao, R. Su, L. Zhang, S. Chen, Y. Zhao, A. Huan, E. H. Sargent, Q. Xiong, H. V. Demir, *Nano Lett.* **2018**, *18*, 3157.

[241] P. Vashishtha, M. Ng, S. B. Shivarudraiah, J. E. Halpert, *Chem. Mater.* **2019**, *31*, 83.

[242] G. Pan, X. Bai, W. Xu, X. Chen, Y. Zhai, J. Zhu, H. Shao, N. Ding, L. Xu, B. Dong, Y. Mao, H. Song, *Nanoscale*, **2020**, *12*, 11728.

[243] N. Yantara, N. F. Jamaludin, B. Febriansyah, D. Giovanni, A. Bruno, C. Soci, T. C. Sum, S. Mhaisalkar, N. Mathews, *ACS Energy Lett.* **2020**, *5*, 1593.

[244] M. L. Lai, T. Y. S. Tay, A. Sadhanala, S. E. Dutton, G. Li, R. H. Friend, Z. K. Tan, *J. Phys. Chem. Lett.* **2016**, *7*, 2653.

[245] W. L. Hong, Y. C. Huang, C. Y. Chang, Z. C. Zhang, H. R. Tsai, N. Y. Chang, Y. C. Chao, *Adv. Mater.* **2016**, *28*, 8029.

[246] X. Zhang, C. Wang, Y. Zhang, X. Zhang, S. Wang, M. Lu, H. Cui, S. V. Kershaw, W. W. Yu, A. L. Rogach, *ACS Energy Lett.* **2019**, *4*, 242.

[247] Z. Wang, F. Wang, B. Zhao, S. Qu, T. Hayat, A. Alsaedi, L. Sui, K. Yuan, J. Zhang, Z. Wei, Z. Tan, *J. Phys. Chem. Lett.* **2020**, *11*, 1120.

[248] Z. Guo, J. Li, R. Pan, J. Cheng, R. Chen, T. He, *Nanoscale* **2020**, *12*, 15560.

**ADVANCED
SCIENCE NEWS**

www.advancedsciencenews.com

**ADVANCED
PHOTONICS
RESEARCH**
Open Access

www.adpr-journal.com

Maning Liu received his Ph.D. degree (2017) in physical chemistry from Royal Melbourne Institute of Technology (RMIT), Australia. He worked as a senior process engineer for 7 years in the industry of semiconductors and solar cells, in China, prior to his Ph.D. research. He then completed postdoctoral research at RMIT from 2017 to 2018. He is currently a postdoctoral researcher at the Faculty of Engineering and Natural Sciences, Tampere University (TAU), Finland. His current research interests cover the preparation, understanding, and applications of novel semiconductor functional materials such as PNCs in third-generation solar cells and photocatalysis.

Paola Vivo is an associate professor at Tampere University (TAU). After pursuing her Ph.D. in chemistry, she received the Academy of Finland Fellowship for postdoctoral research, in 2013–2017. She currently leads the Hybrid Solar Cells group (https://research.tuni.fi/hsc/) at the Faculty of Engineering and Natural Sciences at TAU. Her research interests include developing solution-processable organic semiconductors and hybrid organic–inorganic systems for third-generation solar cells, with main emphasis on lead-free halide perovskites in bulk and nanocrystals.